

# Chemical controls on incipient Mg-silicate crystallization at 25°C: Implications for early and late diagenesis

N. J. TOSCA<sup>1,\*</sup> AND A. L. MASTERSON<sup>2</sup>

<sup>1</sup> Department of Earth and Environmental Sciences, University of St Andrews, St Andrews, KY16 9AL, UK, and

<sup>2</sup> Department of Earth and Planetary Sciences, Harvard University, Cambridge, MA 02138, USA

(Received 11 March 2013; revised 29 May 2013; Editor: Tony Fallick)

**ABSTRACT:** Mg-silicate minerals (e.g., stevensite, kerolite, talc, sepiolite) play an important role in the construction of facies models in lacustrine and peri-marine environments because they are sensitive to changes in solution chemistry. However, the response of Mg-silicate mineralogy to changing aqueous chemistry is only broadly understood because the mechanisms underpinning the co-precipitation of Mg<sup>2+</sup> and SiO<sub>2</sub>(aq) from surface water, and subsequent Mg-silicate crystallization, are unclear. Here we describe the results of experiments designed to systematically examine the effects of pH, Mg/Si and salinity of the parent solution on the nature of initially precipitated products. Structural interrogation of the products with X-ray diffraction (XRD), Fourier-transform infrared spectroscopy (FTIR) and thermal analysis (TGA/DTA) allow comparison of synthetic products with naturally occurring crystalline counterparts. In general, Mg<sup>2+</sup> and SiO<sub>2</sub>(aq) co-precipitation and nucleation of Mg-silicate layer structures first involves the rapid formation of 2:1 layers with trioctahedral occupancy and a mean coherent X-ray scattering domain between 1–2 unit cells with respect to the *c* axis. Well defined but diffuse *hk* reflections indicate two-dimensional growth, turbostratic stacking and highly variable interlayer hydration. Diffuse reflectance FTIR shows numerous structural similarities with stevensite, kerolite and sepiolite. However, TGA/DTA analysis indicates the presence of variable kerolite/stevensite interstratification not readily detectable through XRD analyses, as well as a significant degree of surface and interlayer hydration (e.g. 15–20 wt.%).

We observe a number of clear trends in the products with respect to solution chemistry. For example, at low salinity, kerolite-like products dominate at high Mg/Si and high pH, whereas sepiolite-like products are formed at lower pH and lower Mg/Si. At high salinity and high Mg/Si, stevensite-like products are favoured at high pH and kerolite-like products dominate at lower pH, whereas a decrease in Mg/Si of the solution leads to sepiolite-like products at low pH and only stevensite-like products at high pH. Higher pH leads to an increase in octahedral vacancies which favour stevensite-like products; this may result from a higher rate of two-dimensional tetrahedral sheet expansion relative to the octahedral sheet, as inferred from studies of silica oligomerization and brucite growth kinetics.

Together, our results indicate that the neoformation of Mg-rich silicates from solution may often begin with the rapid nucleation of hydrated 2:1 layers. Subsequent dehydration leads to progressive layer stacking order and could occur in response to wetting/drying cycles, prolonged exposure to high salinity solutions, or burial and heating. The surface and interlayer water associated with these products is undoubtedly an important source of diagenetic water in Mg-silicate-bearing successions, and the chemistry of this water upon later diagenesis should be a focus of future investigation.

**KEYWORDS:** diagenesis, lacustrine, stevensite, kerolite, sepiolite, synthesis.

\* E-mail: njt6@st-andrews.ac.uk

DOI: 10.1180/claymin.2014.049.2.03

Mg-rich phyllosilicate minerals (e.g. stevensite, kerolite, talc) and modulated phyllosilicates (e.g. sepiolite) are commonly precipitated directly from surface water. Because minerals formed in this way often record primary solution composition and its fluctuation over time, Mg-silicates have played a prominent role in the construction of facies models in modern and recent lacustrine settings, epicontinental and inland seas and lakes, and marine environments (e.g. Millot, 1970; Jeans, 1971; Weaver & Beck, 1977; Stoessell & Hay, 1978; Bodine, 1983; Jones & Weir, 1983; Callen, 1984; Bertani & Carozzi, 1985; Jones, 1986; Webster & Jones, 1994; Calvo *et al.*, 1999; Chahi *et al.*, 1999; Deocampo, 2004; Deocampo *et al.*, 2009; Jones & Conko, 2011; Bristow *et al.*, 2012; Clauer *et al.*, 2012). In fact, Hardie & Eugster (1970) and Eugster & Jones (1979) recognized early on that Mg-silicates act as early evaporative precipitates creating critical “chemical divides” in the chemical evolution of closed basin brines, but considered the relative timing of these reactions problematic. In addition, the utility of Mg-silicate minerals may be extended through geologic time if their burial diagenetic reactions can be unravelled (Millot & Palausi, 1959; Noack *et al.*, 1989; Macdonald *et al.*, 2011; Tosca *et al.*, 2011; Macdonald *et al.*, 2012). Beyond problems in Earth history, knowledge of Mg-silicate neof ormation processes in non-marine carbonate hydrocarbon reservoirs will also enable predictions of burial and later diagenetic reactions, their effects on pore fluid chemistry and therefore influences on hydrocarbon reservoir properties (Tettenhorst & Moore, 1978; Bertani & Carozzi, 1985; Wright, 2012).

The response of Mg-silicate distribution to evolving surface water chemistry and climate through space and time, however, is still only understood at a broad level. This problem persists largely because the mechanisms underpinning the link between solution chemistry and Mg-silicate mineralogy are not clear. Thermodynamic treatment of the Mg-silicate system provides an important starting point. Studies on the relative stabilities of stevensite, kerolite and sepiolite show that, in line with field observations, salinity should dictate the presence of stevensite versus sepiolite, and that pH and Mg/Si should also play important roles (Jones, 1986; Jones & Galan, 1988; Stoessell, 1988; Birsoy, 2002; Jones & Conko, 2011). What this work also shows, however is that all of these minerals are metastable to talc at  $\text{SiO}_2(\text{aq})$  of marine and surface

waters, and their solubilities are similar to one another, implicating kinetic controls in the dominance of one Mg-silicate phase over another in Al-free systems (Hostetler & Christ, 1968; Velde, 1985; Jones, 1986; Stoessell, 1988; Jones & Galan, 1988).

Experimental studies of Mg-silicates offer an additional perspective. Some of these have utilized methods relevant to natural Mg-silicate formation, including for example, initiating precipitation by evaporation or by modifying solution chemistry, and gel crystallization (e.g. Siffert & Wey, 1962; Wollast *et al.*, 1968; Couture, 1977; La Iglesia, 1978; Decarreau, 1980; Abtahi, 1985; Decarreau, 1985; Tosca *et al.*, 2011; Decarreau *et al.*, 2012). A few studies have successfully documented changes in product identity in response to solution chemistry (e.g. Siffert & Wey, 1962; La Iglesia, 1978), but in general, problems with characterising often poorly crystalline materials that result from aqueous precipitation have made comparison of results difficult. In addition, similar precipitation rates and the polyphase products that are typically produced from this type of experiment preclude the determination of solubility products for a specific phase. Despite this, experimental results have confirmed broad field relationships and illuminate the possible kinetic barriers involved. The studies also suggest that the formation of Mg-silicates from solution is a complex process, often involving the formation of poorly crystalline intermediates that may influence the development of crystalline phases (Strese & Hofmann, 1941; Wollast *et al.*, 1968; Mitsuda & Taguchi, 1977; Williams *et al.*, 1985; Jones, 1986; Packter, 1986; Takahashi *et al.*, 1994; Tosca *et al.*, 2011). Indeed, as we discuss in more detail below, there is much evidence that the process of Mg-silicate formation from solution involves such poorly crystalline intermediates and that these materials are transferred to the sedimentary record where they are susceptible to a range of diagenetic reactions.

Here we discuss an experimental programme aimed at understanding the initial steps and products involved in Mg-silicate neof ormation at 25°C. The experiments examine the precipitation of  $\text{Mg}^{2+}$  and  $\text{SiO}_2(\text{aq})$  from synthetic solutions designed to be similar to waters found in saline alkaline environments. Consequently, the focus of this work is to identify and characterize incipient products produced as a function of solution chemistry and their relationship to crystalline Mg-

silicate minerals. The experiments systematically examine the effects of pH, Mg/Si and salinity of the parent solution on the nature of initially precipitated products. The disadvantage of this approach relative to previous efforts is the poorly crystalline nature of initially-precipitated material. However, detailed structural characterization is an important focus of this study, helping to illuminate connections between solution and product phases, and diagenetic reactions in which these phases participate.

In what follows, we systematically describe experimental results and piece together the structural characteristics of initially precipitated products in the Mg-silicate system as a function of solution chemistry. We then discuss the relationships between our products and their naturally occurring counterparts. The patterns that emerge in our products as a function of solution chemistry allow us to pose testable hypotheses regarding the mechanistic controls on Mg-silicate mineralogy and their response to environmental parameters. Finally, we discuss the implications of our findings with respect to early and later diagenetic reactions in Mg-silicate-bearing sedimentary successions.

## EXPERIMENTAL METHODS

All of the experiments described here were conducted as batch experiments in 1 litre high density polyethylene (HDPE) bottles. Solutions were prepared first by addition of  $\text{SiO}_2(\text{aq})$  to deionized water at fixed pH. The source of aqueous silica used in the experiments was a 99.9% reagent-grade anhydrous tetraethoxysilane (or TEOS) solution, which upon contact with water rapidly hydrolyzes, producing  $\text{SiO}_2(\text{aq})$  and residual ethanol. After the hydrolysis of TEOS, a small amount of ethanol remains in solution, but engages in negligible complexing with  $\text{Mg}^{2+}$ . However, although the hydrolysis of organo-silica complexes is rapid, there is a well-documented lag period during which the initially introduced  $\text{SiO}_2(\text{aq})$  reaches equilibrium with the ambient solution (Iler, 1979; Dietzel, 2000). With this in mind, all  $\text{SiO}_2(\text{aq})$  introduced in the experiment was given enough time to de-polymerize and equilibrate in the solution (typically 24 h) before  $\text{Mg}^{2+}$  was introduced by the addition of known amounts of  $\text{MgCl}_2(\text{aq})$ . The start of the experiment was taken as the addition of  $\text{MgCl}_2(\text{aq})$  to the vessels. Upon  $\text{MgCl}_2(\text{aq})$  addition, crystallization was evident in little less than an hour to as long as 48 h from the

start of the experiment. When a precipitate was formed, the solution took on a distinct cloudy appearance when stirring, and when stirring stopped the material floated as a translucent gel-like layer at the bottom of the vessels.

All experiments were run at  $25 \pm 0.1^\circ\text{C}$  for a minimum of 4 weeks to a maximum of 7 months, depending on conditions, and were continuously agitated using an orbital shaker. The pH in all experiments was buffered to the desired value by the addition of the TRIS buffer (*tris*(hydroxymethyl)aminomethane) and HCl. Complexing between the TRIS buffer and  $\text{Mg}^{2+}(\text{aq})$  is negligible; however this is not the case with other transition metal ions (Fischer *et al.*, 1979). Over the course of the experiments pH was continuously monitored to ensure values remained in the targeted range (no more than 0.05 units from the initial set value,  $\text{pH}_i$ ). Conditions of the experiments are listed in Table 1.

Before experiment termination, the solution was sampled for analysis and passed through a 0.1  $\mu\text{m}$  nylon syringe filter into pre-acidified vials. The remaining solution was filtered through a 0.1  $\mu\text{m}$  nylon filter membrane using a vacuum filtration apparatus. Solid precipitates were thoroughly washed with deionized water during the filtration process in order to remove any dissolved components. The solid precipitate was left on the filter as a translucent white gel and the filter cake was slowly dried in a  $50^\circ\text{C}$  oven for 7–14 days. Drying of the gel is particularly sluggish under these conditions, and when drying was complete the material was lightly crushed in an agate mortar and pestle and prepared for further analysis.

## ANALYTICAL METHODS

Powder X-ray diffraction (XRD) data were collected using a Siemens D500 X-ray diffractometer using  $\text{Co-K}\alpha_1$  radiation. Operating conditions were 40 kV and 20 mA and divergent and receiving slit sizes of  $1^\circ$  were used. Data were collected between  $5\text{--}80^\circ$   $2\theta$  with a step size of  $0.02^\circ$  and a counting time of 5 s per step. Samples were backloaded into bulk powder holders and therefore assumed to be presented to the X-ray beam in a randomly oriented state. Because of the nature of the gel upon wetting and limited amount of sample, attempts were not made to prepare oriented specimens for XRD.

FTIR analyses on powdered products were acquired in diffuse reflectance mode using a Bruker

IFS 66v infrared spectrometer. FTIR measurements were collected on KBr pellets with a sample:KBr ratio of approximately 1:300. Measurements were collected from 400–4000  $\text{cm}^{-1}$  at 1  $\text{cm}^{-1}$  resolution using a DTGS detector with a KBR window and beam splitter.

Thermogravimetric and differential thermal analyses (TG/DTA) were performed with a Netzsch STA 449c Jupiter thermo-microbalance housed in the School of Chemistry at the University of St Andrews. All experiments were conducted in air at a flow rate of 40 mL/min from 35°C to 1050°C at a heating rate of 5°C/min. Samples were contained in an  $\text{Al}_2\text{O}_3$  crucible and all experiments utilized a SiC furnace as well as  $\text{Al}_2\text{O}_3$  as a reference material.

ICP-MS analyses were performed on initial and final solution samples to determine the concentrations of  $\text{Na}^+$ ,  $\text{Mg}^{2+}$ , and  $\text{SiO}_2(\text{aq})$  at the outset and the conclusion of each experiment. All samples were diluted to appropriate levels using an  $\text{HNO}_3$  matrix and calibrated using a Varian Vista Pro simultaneous ICP-AES. Calibration was performed with eight standard solutions bracketing expected sample concentrations. In addition, two external quality control standards (matrix matched) were periodically analysed with samples to determine external precision (0.44% relative standard deviation for Mg and Si, and 0.69% for Na) and accuracy (0.57–1.03%).

Finally, thermodynamic analysis of solution compositions was performed to obtain ionic strength (Table 1) and assess the state of saturation with respect to various mineral phases. These were performed with Geochemist's Workbench software (Bethke, 2002). We used an activity model constructed using a Pitzer-based method for ion activity coefficient calculation based on models developed by Harvie *et al.* (1984) and Marion & Farren (1999) for major seawater components at high ionic strength. For silica speciation in solution, we included  $\text{H}_4\text{SiO}_4$  dissociation constants from Hershey & Millero (1986) and Pitzer coefficients for  $\text{SiO}_2(\text{aq})$  species as well as stability constants for aqueous silica complexes calculated by Felmy *et al.* (2001). Data reported in the Felmy *et al.* (2001) study are based on solution NMR analyses of concentrated  $\text{SiO}_2(\text{aq})$  and  $\text{Na}^+$ -bearing solutions. Speciation calculations referred to in the text were conducted by specifying initial or final pH values and total  $\text{SiO}_2(\text{aq})$ ,  $\text{Mg}^{2+}$  and  $\text{Na}^+$  concentrations. Calculations also assumed equilibrium with a  $\text{CO}_2$ -

containing atmosphere at a  $\log f_{\text{CO}_2} = -3.5$  (corresponding to ambient atmosphere).

## RESULTS

Below we systematically discuss the results of experiments run at low salinity and high salinity by modifying initial background electrolyte ( $\text{NaCl}_i$ ) concentration. For each salinity, variable pH experiments (at  $\text{pH}_i$  8.7, 9.0 and 9.4) were run at three  $\text{Mg}/\text{Si}_i$  values: high (5–7), medium (~1), and low (~0.67).

To be clear, the products formed in our experiments are synthetic and therefore cannot, by definition, be referred to as minerals or by their mineral names. Instead our products are best described as Mg-silicate precipitates which, as we discuss in more detail below, share a number of structural similarities with crystalline Mg-silicate minerals. For the purposes of discussion, if a material possesses sufficient structural similarities with a naturally-occurring mineral, for example, kerolite, we use the term “kerolite-like” to describe our product (Guggenheim *et al.*, 2002, 2006).

### *Low-salinity experiments ( $\text{NaCl}_i = 0.0\text{mol/kg}$ )*

*Variable pH at  $\text{Mg}/\text{Si} = 6$ .* X-ray powder diffraction of materials extracted at high  $\text{Mg}/\text{Si}$  and low salinity show progressively increasing definition of *hkl* reflections with increasing pH. These peaks occur at approximately 4.4, 3.3, 2.6 and 1.52–1.53 Å (Fig. 1a). A low-angle peak that might indicate a basal 001 reflection is not observed from raw data, but further insight can be gained from examination of calculated differences in XRD patterns between samples. These differences indicate a weak increase in X-ray scattering corresponding to an apparent *d* spacing of ~10 Å (Fig. 2a). In addition, as pH increases, a broad diffuse band located at ~4.0 Å decreases, which reflects the occurrence of amorphous silica at low pH and its absence as pH increases. Together, the *hkl* peak positions and the weak increase in X-ray scattering at ~10 Å as pH increases are consistent with a Mg-silicate layer structure, similar to, for example, kerolite.

FTIR spectra collected on these materials are consistent with XRD data, but also offer further insight into subtle structural differences between phases, as well as the occurrence of multiple products. As a general consequence of small

TABLE 1. Experimental conditions.

Experiment	pH <sub>i</sub>	Na <sub>i</sub> (mg/kg)	Mg <sub>i</sub> (mg/kg)	SiO <sub>2</sub> (aq) <sub>i</sub> (mg/kg)	Mg/Si <sub>i</sub> (mol/mol)	Ionic strength (m)
MgSi6-A	8.65	18	1290	460	6.9	0.16
MgSi6-B	8.95	9.4	1290	538	5.9	0.15
MgSi6-C	9.36	3.7	1290	641	5.0	0.13
MgSi1-A	8.67	2.9	243	460	1.3	0.03
MgSi1-B	8.97	3.3	243	538	1.1	0.03
MgSi1-C	9.38	2.3	243	641	0.9	0.03
MgSi07-A	8.53	22	122	460	0.7	0.02
MgSi07-B	8.83	8.4	143	538	0.7	0.02
MgSi07-C	9.36	5.4	172	641	0.7	0.02
MgSi6-D	8.67	12200	1290	460	6.9	0.67
MgSi6-E	8.95	13220	1290	538	5.9	0.73
MgSi6-F	9.36	15580	1290	641	5.0	0.82
MgSi1-D	8.68	12460	243	460	1.3	0.57
MgSi1-E	8.95	12080	243	538	1.1	0.57
MgSi1-F	9.37	12530	243	641	0.9	0.58
MgSi07-D	8.66	13640	122	460	0.7	0.61
MgSi07-E	8.93	13590	143	538	0.7	0.61
MgSi07-F	9.35	15420	172	641	0.7	0.70

particle size and low crystallinity, FTIR bands are broadened, which causes individual absorptions to coalesce (Farmer, 1974a). As is the case with all samples examined here, the region from 3000–4000 cm<sup>-1</sup> shows a number of absorptions, suggesting complex and variable hydration (Fig. 3a). At high Mg/Si and low salinity, all products show an absorption at ~3680 cm<sup>-1</sup>, a broad absorption centred at ~3430 cm<sup>-1</sup> which are attributed to Mg<sub>3</sub>-OH vibrations from the trioctahedral sheet and OH stretching associated with interlayer or surface-bound water (Wilkins & Ito, 1967; Farmer, 1974b), respectively (Fig. 3a). Weak shoulders centred at approximately 3620 and 3250 cm<sup>-1</sup> are also present in this region and are most consistent with absorptions arising from interlayer water (Wilkins & Ito, 1967; Farmer, 1974b; Russell & Fraser, 1994).

The region between ~400–1400 cm<sup>-1</sup> yields additional information regarding lattice vibrations (Figs 4 and 5). For samples with high Mg/Si and low salinity, the main absorption at 1024 cm<sup>-1</sup> results from Si–O stretching and is relatively constant in samples across the pH range from 8.7 to 9.4 (Fig. 4a). This feature, as well as the less intense absorption at ~910 cm<sup>-1</sup>, is representative of layer silicate structures, specifically 2:1 varieties similar to talc, kerolite and trioctahedral smectites (Faust *et al.*,

1959; Wilkins & Ito, 1967; Farmer, 1974b; Brindley *et al.*, 1977; Russell & Fraser, 1994). The product formed at pH 8.7 also exhibits a weak shoulder positioned at approximately 1210 cm<sup>-1</sup>. Of all of the silicate mineral lattice vibrations only sepiolite is known to exhibit a Si–O vibration feature in this range; this is a result of the periodic inversion of Si tetrahedra in the 2:1 layer (Farmer, 1974a). Other lattice vibrations are observed for all three materials at ~450–470 and 660–677 cm<sup>-1</sup>, which include the translational and librational OH vibrations, respectively, as well as other Si–O vibrations (Fig. 5a). As is the case with hydroxyl and water vibrations, these vibrations are consistent with a trioctahedral layer silicate structure similar to that of kerolite (Brindley *et al.*, 1977). However, aside from the indication of a weak feature indicative of sepiolite, the material formed at pH 8.7 also includes a weak vibration centred at ~800 cm<sup>-1</sup>, which indicates the presence of amorphous silica.

In general, thermogravimetric (TG) analysis of precipitated products formed at high Mg/Si and low salinity show an increasing level of total hydration with increasing pH (Table 2). Derivative (DTG) curves show a strong weight loss event at ~100–130°C and much weaker events at ~235, 450–500 and 730–830°C (Fig. 6a). Again, this array of features speaks to the complex nature of

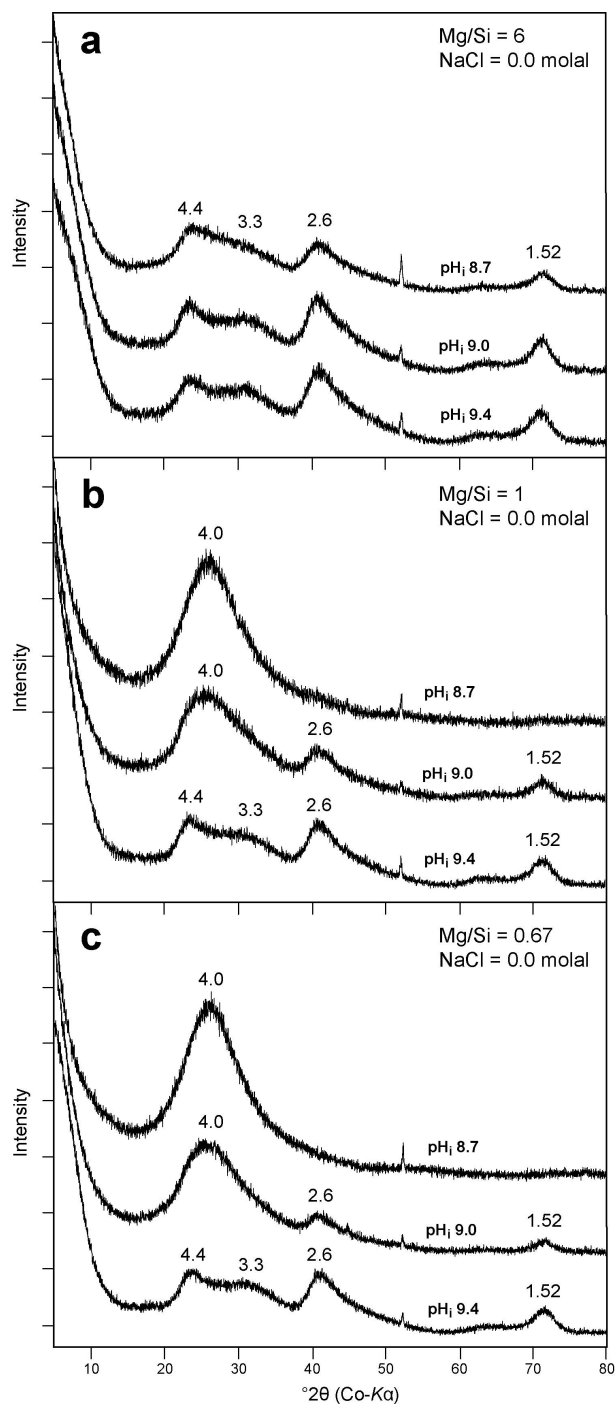


FIG. 1. Representative powder XRD patterns of products formed at low salinity ( $\text{NaCl} = 0.0 \text{ mol/kg}$ ) and (a)  $\text{Mg/Si} = 6$  (b)  $\text{Mg/Si} = 1$  (c)  $\text{Mg/Si} = 0.67$ . At all  $\text{Mg/Si}$  values,  $hkl$  peaks become more intense as pH increases. Higher  $\text{Mg/Si}$  values favour the development of 2:1 layer structures at lower pH. The sharp reflection at  $\sim 53^\circ$  is due to the aluminium sample holder (SH).

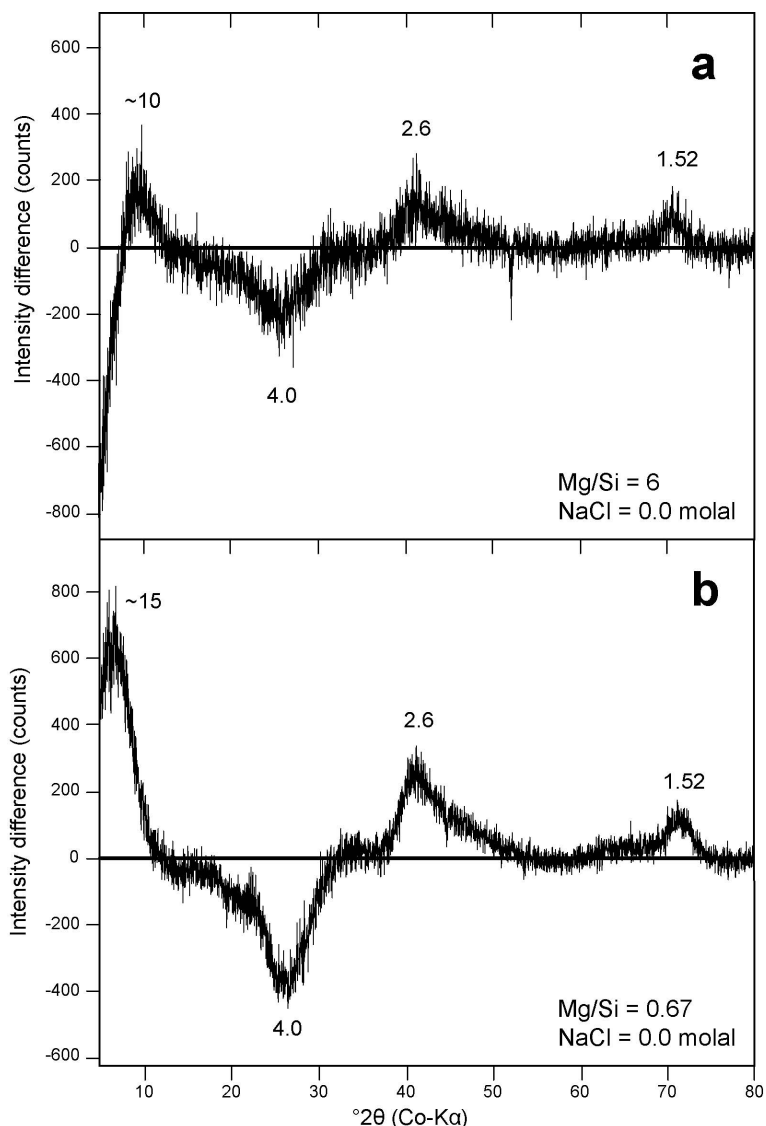


FIG. 2. Differences in XRD intensity between precipitates formed at low and high pH. (a) Calculated difference between precipitates formed at pH 8.7 and pH 9.0 at Mg/Si = 6 and low salinity. Increases in intensity at  $\sim 10$ , 2.6 and 1.52 Å indicate the growth of a layered silicate with a kerolite-like structure, while decreases at 4.0 Å indicate loss of amorphous silica. (b) Calculated difference between precipitates formed at pH 8.7 and 9.4 at Mg/Si = 1 and high salinity. Increases in intensity at  $\sim 15$ , 2.6 and 1.52 Å indicate the growth of a layered silicate with a stevensite-like structure, while decreases at 4.0 Å indicate loss of amorphous silica.

hydration and a generally poorly crystalline nature resulting in protracted dehydroxylation (Bish & Duffy, 1990). In general, the temperature of the first dehydration event increases as pH increases, which, if the materials are dominantly composed of the same phase, suggests an increasing degree of

crystallinity. DTA curves of the same experiments indicate that the first two dehydration events are endothermic, reflecting loss of adsorbed and interlayer water (Table 2).

The DTA curves also show a very broad endothermic feature from  $\sim 600$ – $900^\circ\text{C}$  which

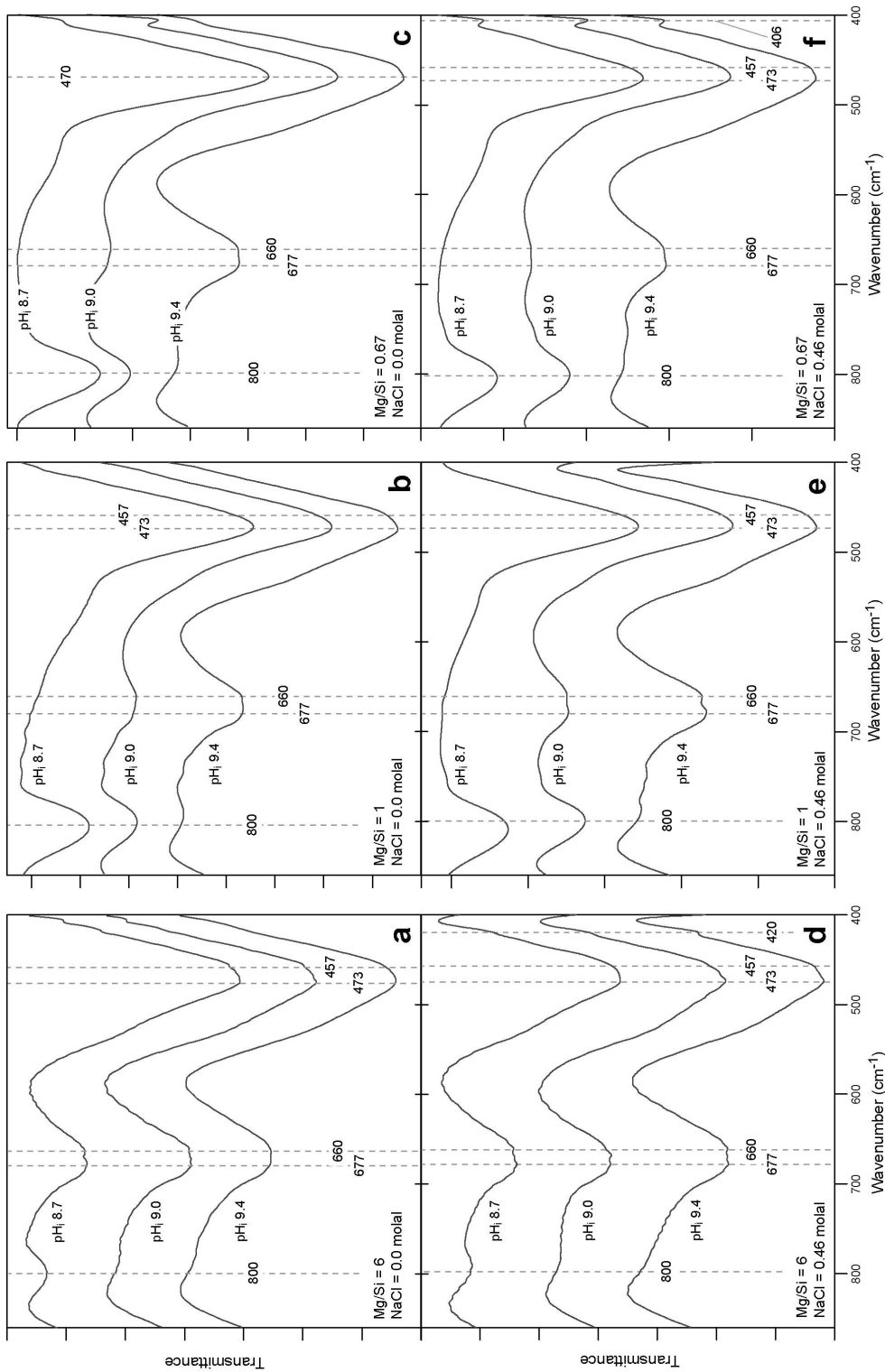


Fig. 3. Hydroxyl stretching region of FTIR spectra acquired on products formed at low salinity ( $\text{NaCl} = 0.0$  mol/kg) and (a)  $\text{Mg/Si} = 6$  (b)  $\text{Mg/Si} = 1$  (c)  $\text{Mg/Si} = 0.67$  and high salinity ( $\text{NaCl} = 0.46$  mol/kg) and (d)  $\text{Mg/Si} = 6$  (e)  $\text{Mg/Si} = 1$  (f)  $\text{Mg/Si} = 0.67$ .

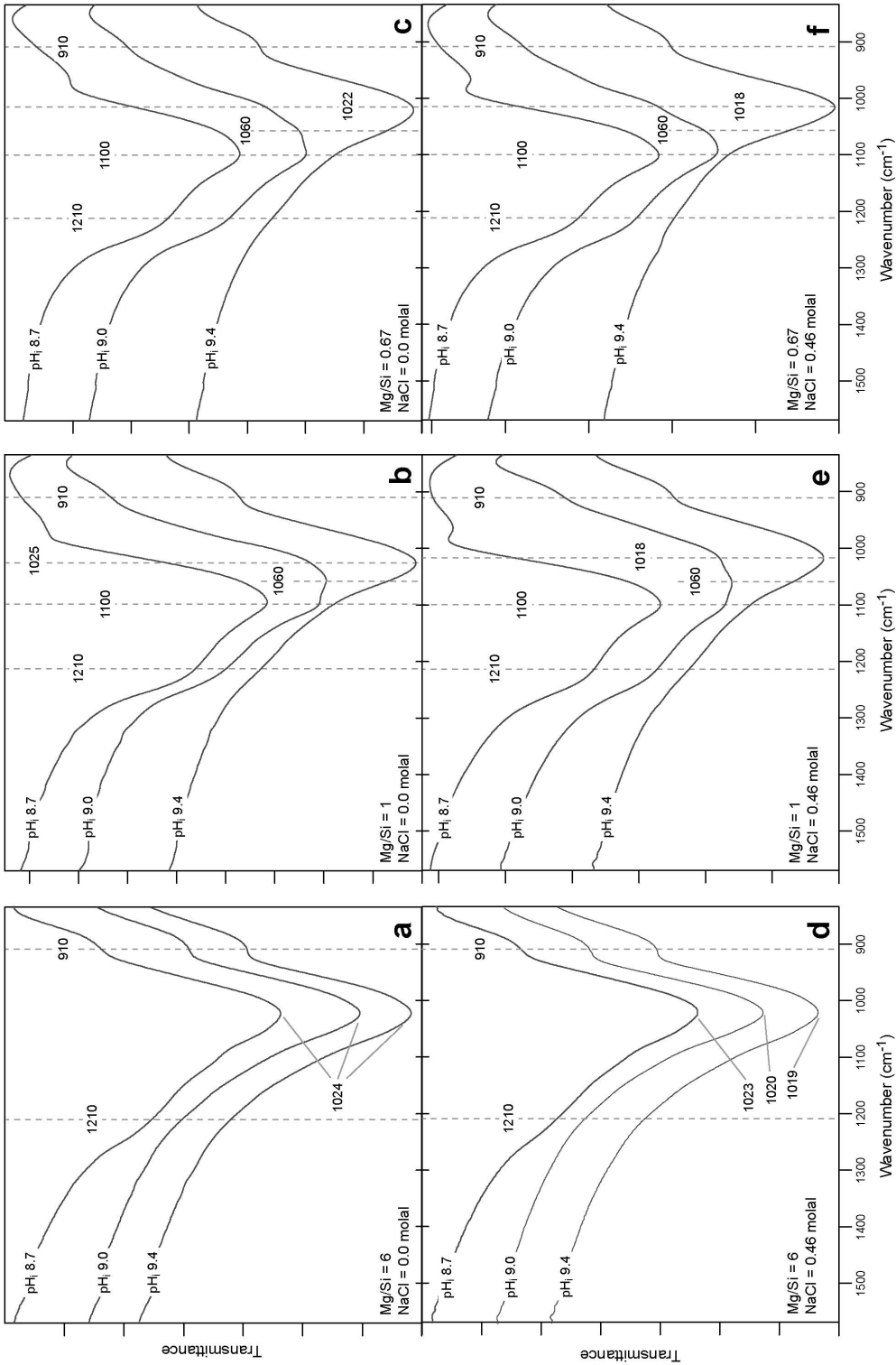


FIG. 4. Lattice vibration region of FTIR spectra (800–1600 cm<sup>-1</sup>) acquired on products formed at low salinity (NaCl = 0.0 mol/kg) and (a) Mg/Si = 6 (b) Mg/Si = 1 (c) Mg/Si = 0.67 and high salinity (NaCl = 0.46 mol/kg) and (d) Mg/Si = 6 (e) Mg/Si = 1 (f) Mg/Si = 0.67.

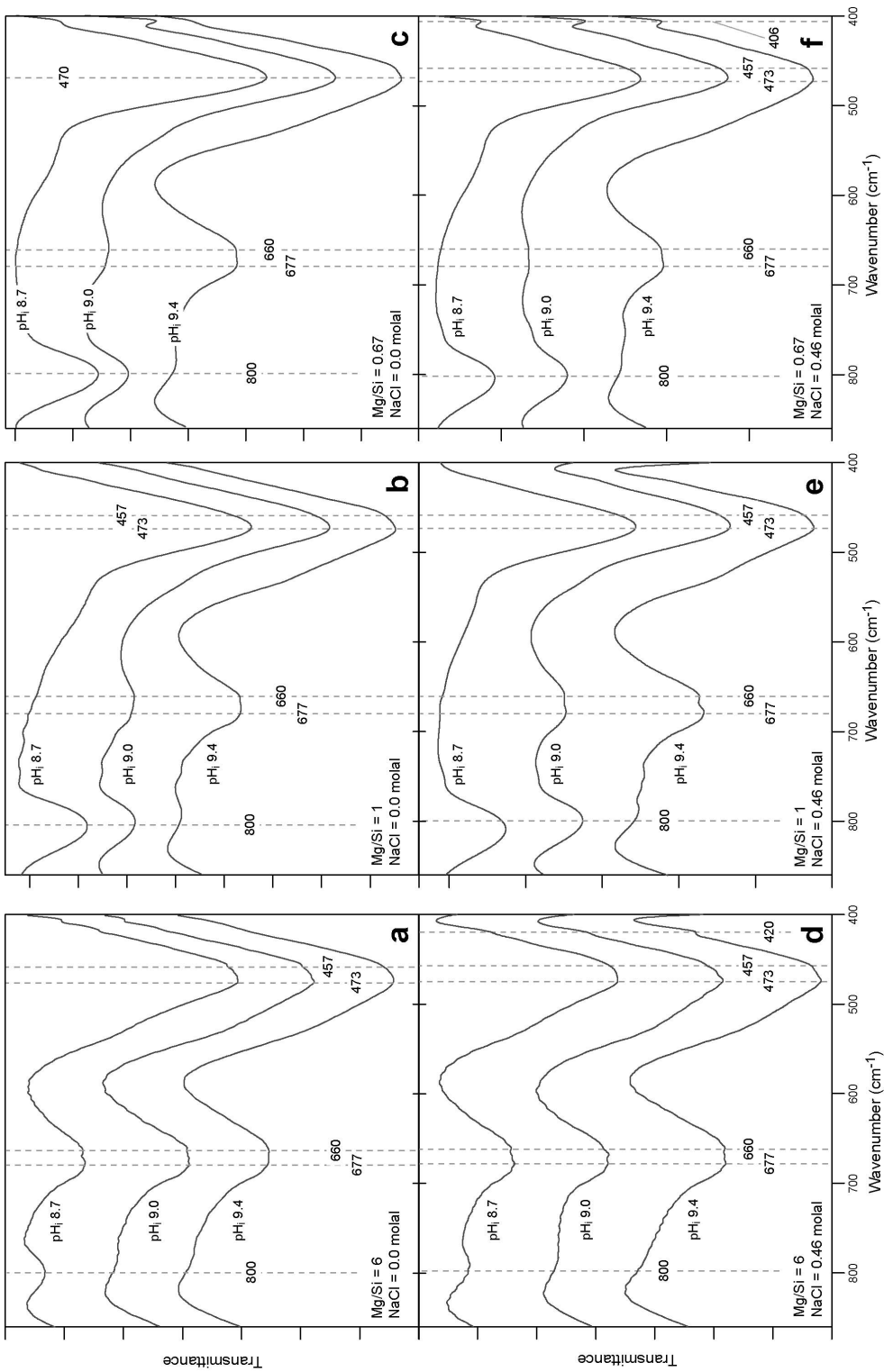


FIG. 5. Lattice vibration region of FTIR spectra (400–900  $\text{cm}^{-1}$ ) acquired on products formed at low salinity (NaCl = 0.0 mol/kg) and (a) Mg/Si = 6 (b) Mg/Si = 1 (c) Mg/Si = 0.67 and high salinity (NaCl = 0.46 mol/kg) and (d) Mg/Si = 6 (e) Mg/Si = 1 (f) Mg/Si = 0.67.

TABLE 2. TGA and DTA data for synthetic products.

Experiment	Total wt. loss (%)	WL		— Endotherms (°C) —			Exotherms (°C)	
		<400°C (%)	>400°C (%)					
MgSi6-A	20	12.3	7.7	121		840		855
MgSi6-B	21.5	12.7	8.8	122		725; 823	749	847
MgSi6-C	22.1	13.2	8.9	143; 270		728; 803	752	827; 849
MgSi1-A	11.3	7.5	3.8	119		730; 843		871
MgSi1-B	11.9	7.2	4.7	128		850		871
MgSi1-C	14.5	9.1	5.4	129		729; 850		853
MgSi07-A	11.9	8.3	3.6	127; 287	426; 570; 636	729; 839		870
MgSi07-B	22	17.2	4.8	95		796	812	870; 971
MgSi07-C	30.1	24.3	5.8	120; 280	659	830	780	852
MgSi6-D	20	14.3	5.7	114		818		844
MgSi6-E	20.8	11.7	9.1	123	677	807; 827	711; 764	
MgSi6-F	21	13.8	7.2	130	688	845	727; 792	
MgSi1-D	12.8	8.1	4.7	126; 287	622			837; 870; 919
MgSi1-E	12.1	8.8	3.3	125	432; 607	831	812	854; 965
MgSi1-F	22.4	14.1	8.3	119; 190	654	762; 818	712; 792	870
MgSi07-D	8.7	6.1	2.6	118		717; 988		871; 910
MgSi07-E	22.4	17.8	4.6	101				916
MgSi07-F	29.2	23.9	5.3	124	663	763; 839	716; 783	

likely reflects the protracted dehydroxylation and small crystal size of these materials (Mackenzie, 1970a; Smykatz-Kloss, 1974) (Fig. 6b; maxima are listed in Table 2). Importantly, strong sharp exothermic peaks are observed from ~800–840°C for each of the three samples, with the samples at the two highest pH levels exhibiting multiple exothermic events. The high-temperature exotherm is assigned to the breakdown of the kerolite-like structure and the subsequent recrystallization of enstatite and forsterite. Indeed, similar exothermic reactions were reported from DTA analysis of natural kerolite from Hawaii (Leveille *et al.*, 2002). Additional weak exothermic inflections are also present in the two higher pH samples at ~750°C which, as we discuss below, is consistent with small amounts of stevensite-like material occurring as an interstratification among dominantly kerolite-like material (Fig. 6b).

In summary, XRD, FTIR and TGA/DTA analyses show that high Mg/Si and low salinity favour the production of a phase identical to poorly crystalline kerolite. The role of pH appears to be somewhat minor across the range studied, with the occurrence of minor sepiolite-like material and amorphous silica at pH 8.7. The kerolite-like product may

contain small amounts of expandable interstratification (e.g. stevensite-like phase).

*Variable pH at Mg/Si = 1.* Products extracted from experiments run at an Mg/Si of 1 and low salinity show significant differences from those formed at higher Mg/Si levels. Firstly, powder XRD analyses show that at low pH, *hkl* peaks corresponding to layered silicate structures are no longer observed (Fig. 1b). At pH 8.7, a single broad band corresponding to the presence of amorphous material is observed at ~4.0 Å. As pH is increased to 9.0, additional *hkl* peaks appear at 2.6 and 1.52 Å. Finally, at pH 9.4, *hkl* peaks dominate whilst the presence of the amorphous band has decreased significantly. No low-angle peaks corresponding to 001 reflections (or the 110 sepiolite reflection) are observed either in raw data or are clear in patterns calculated by difference between experiments.

The FTIR data also show important differences in products formed at an Mg/Si = 1 compared to an Mg/Si = 6 (Figs 3–5). In the hydroxyl stretching region (Fig. 3b), the 3680 cm<sup>-1</sup> peak corresponding to OH stretching from trioctahedral Mg is only apparent at pH 9.4, very weakly developed at pH 9.0 and absent from the material formed at pH 8.7. In

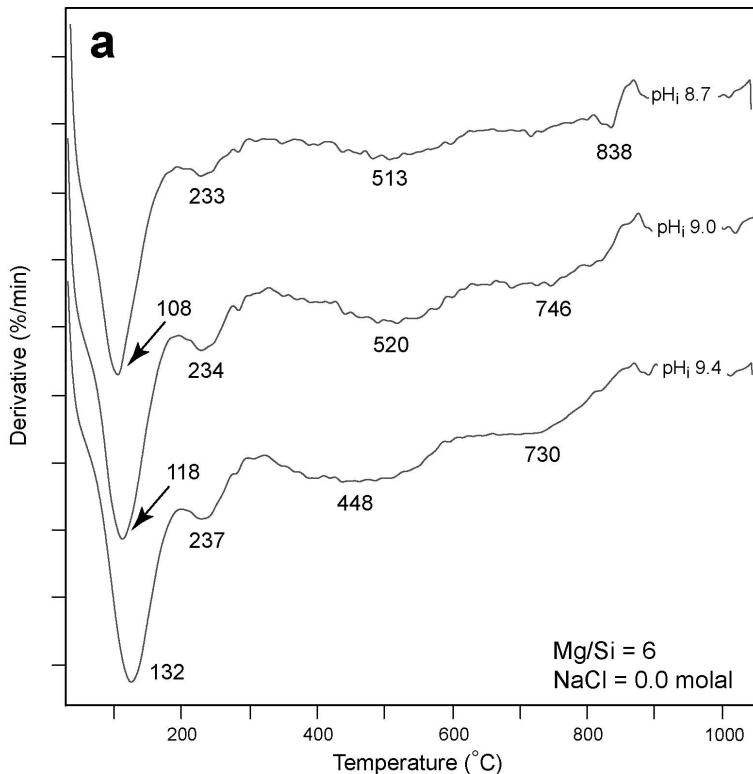


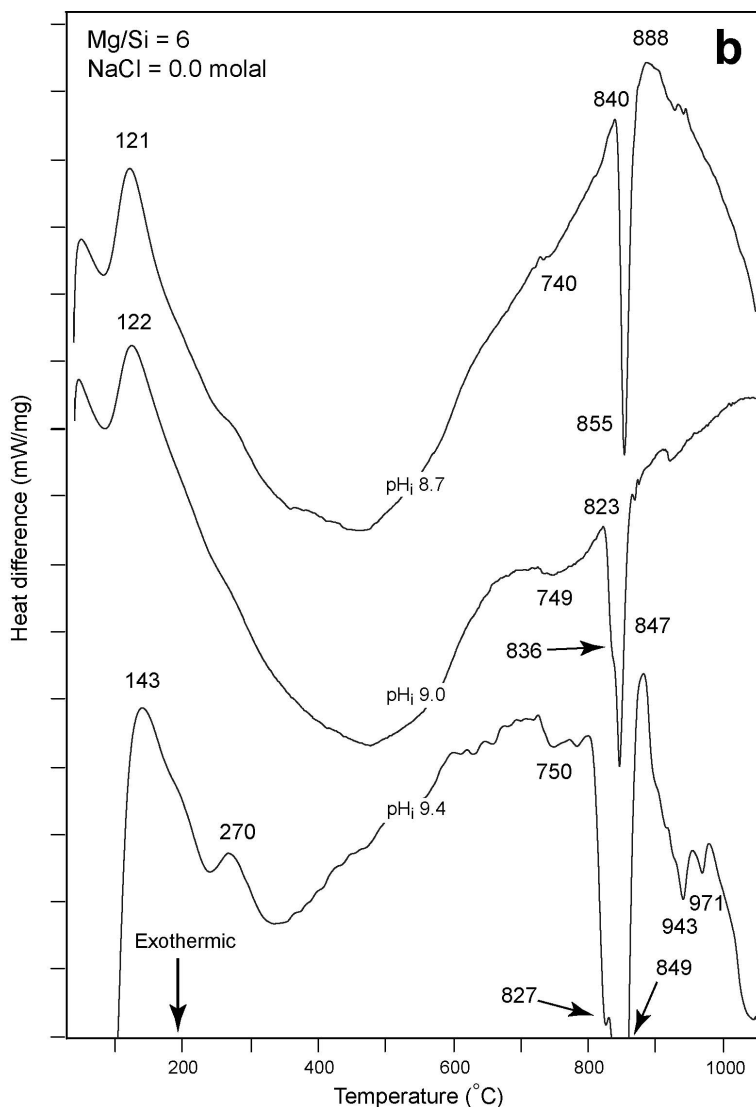
FIG. 6. (a) (*above*) Derivative of the thermal analysis curve (DTG) of products formed at low salinity ( $\text{NaCl} = 0.0$  mol/kg) and  $\text{Mg/Si} = 6$ . As pH increases under these conditions, products exhibit low-temperature weight loss in two steps, as well as a marked shift in dehydroxylation to lower temperatures. (b) (*facing page*) Differential thermal analysis curves of products formed at low salinity ( $\text{NaCl} = 0.0$  mol/kg) and  $\text{Mg/Si} = 6$ . At all pH levels products exhibit protracted endothermic dehydration and dehydroxylation. Exothermic phase transitions remain at  $\sim 850^\circ\text{C}$  in all samples but the growth of a smaller additional exotherm at  $\sim 830^\circ\text{C}$  is evident as pH increases.

addition, the broad absorption present as a shoulder situated at  $\sim 3620\text{ cm}^{-1}$  is only evident from the highest pH experiment and is absent from the low pH experiments. This indicates a much smaller role for interlayer water in the lower pH experiments.

The lattice vibration region of the spectrum also shows noticeable differences when compared to higher  $\text{Mg/Si}$  experiments, particularly among features attributed to Si–O stretching as pH is increased (Fig. 4b). At pH 8.7, the dominant Si–O absorptions are centred at  $\sim 1200$  and  $1100\text{ cm}^{-1}$ . These features are indicative of the presence of a sepiolite-like product and amorphous silica, respectively. As pH is increased to 9.0, these features are present along with an additional feature centred at  $\sim 1060\text{ cm}^{-1}$  which may also arise from a sepiolite-like structure (Russell & Fraser, 1994; Frost *et al.*, 2001). Increasing the experimental pH to 9.4,

however, results in a shift in the dominant absorption to  $1025\text{ cm}^{-1}$ , consistent with a layered 2:1 structure similar to kerolite. The lattice vibration region from  $400\text{--}900\text{ cm}^{-1}$  (Fig. 5b) shows similar trends; the  $800\text{ cm}^{-1}$  absorption attributed to amorphous silica is most intense at low pH and this decreases progressively as pH is increased. Similarly, absorptions at  $677$  and  $660\text{ cm}^{-1}$ , attributed to OH vibrations from octahedral structures progressively increase in intensity with increasing pH.

Compared to products formed at  $\text{Mg/Si} = 6$ , DTA curves of products formed at lower  $\text{Mg/Si}$  exhibit less pronounced two-stage dehydration at low temperature, but more pronounced dehydroxylation at  $\sim 830$  to  $850^\circ\text{C}$ . The low-temperature dehydration is dominated by a mass loss event at  $\sim 85\text{--}110^\circ\text{C}$  which results from the loss of surface-bound water.



However, only in the sample formed at the highest pH is a second dehydration event evident at  $\sim 220^{\circ}\text{C}$ , which likely reflects the loss of inter-layer-bound water from either a kerolite-like or stevensite-like structure (Faust *et al.*, 1959; Kawano & Tomita, 1991).

The DTA curves show that the low-temperature mass loss events are endothermic (Table 2). All three samples also exhibit broad endothermic dehydroxylation events from  $\sim 500$ – $900^{\circ}\text{C}$ . However, the high-temperature exothermic events (assigned to phase transitions) observed for these samples are different from those formed at higher

Mg/Si. In the lowest two pH samples, a sharply defined exothermic event is observed at  $\sim 871^{\circ}\text{C}$  and this immediately follows an endothermic peak at  $\sim 850^{\circ}\text{C}$ . The temperature of this transition is highly consistent but, compared to the exothermic event identified for kerolite-like products described above, the event occurs at a higher temperature. A number of authors have identified exothermic events at similar temperatures for sepiolite and further claim that this can be considered nearly diagnostic; all sepiolites seem to exhibit this transition at comparable temperatures. Martin Vivaldi & Fenoll Hach-Ali (1970) attributed this

event to a phase change from sepiolite to clinoenstatite, which is favoured by the coincidence of the *c* axes of these two phases with respect to length and direction. The presence of this feature in the DTA curve is consistent with FTIR data, suggesting the presence of a sepiolite-like product in these two samples. Therefore we consider this transition to be a reliable indicator of the presence of sepiolite-like materials in subsequent analyses. In contrast to the pH 8.7 and 9.0 experiments that show evidence for similar materials, the product formed at pH 9.4 exhibits a DTA curve similar to kerolite-like products formed at higher Mg/Si. The broad dehydroxylation punctuated by a sharp exothermic transition at  $\sim 850^\circ\text{C}$  indicates the dominance of a kerolite-like phase in this sample (Table 2). Again, similar to other experiments, a broad but weak exothermic inflection is observed at  $\sim 750^\circ\text{C}$  and likely indicates the presence of a small amount of stevensite-like interstratification.

In summary, products generated from pH 8.7 to 9.4 but at an Mg/Si of 1 are dominated by amorphous silica and a sepiolite-like phase at low pH and a kerolite-like phase at pH 9.4. This suggests that high Mg/Si levels in solution favour the formation of kerolite-like materials across a broader range of pH.

*Variable pH at Mg/Si = 0.67.* Powder XRD of products formed at Mg/Si = 0.67 show a number of similarities to those products formed at Mg/Si = 1 (Fig. 1c). The growth of *hkl* reflections increases with increasing pH and this occurs with a simultaneous decrease in the broad  $\sim 4.0$  Å band characteristic of amorphous silica. The *hkl* peaks occur at the same position as those observed in other samples and are indicative of a 2:1 Mg-silicate layer structure (Fig. 1c).

The IR data are consistent with observations from XRD and also bear overall similarity to products formed at Mg/Si = 1. In the hydroxyl stretching region, the absorption centred at  $\sim 3680\text{ cm}^{-1}$ , arising from OH stretching from  $\text{Mg}_3\text{-OH}$  in the trioctahedral sheet, is present only in the highest pH sample (pH 9.4; Fig. 3c). Compared to the same experiment conducted at Mg/Si = 1, the sample formed at Mg/Si = 0.67 shows a less distinct  $3680\text{ cm}^{-1}$  band. Absorptions centred at  $\sim 3250$ ,  $\sim 3430$  and  $\sim 3620\text{ cm}^{-1}$  are all present, as in other samples, but the material formed at the highest pH shows the strongest  $\sim 3620\text{ cm}^{-1}$  band, suggesting the presence of more interlayer  $\text{H}_2\text{O}$  than the other two samples (Fig. 3c).

The lattice vibration region of FTIR spectra for Mg/Si = 0.67 products is also similar to those formed at Mg/Si = 1 with only slight differences in the position of dominant absorptions (Figs 4c and 5c). At the lowest pH of 8.7, a broad shoulder is evident at  $\sim 1200\text{ cm}^{-1}$  along with an absorption positioned at  $\sim 1100\text{ cm}^{-1}$ ; these Si–O absorptions indicate the presence of a sepiolite-like phase and amorphous silica, respectively (Fig. 4c). As pH is increased, these absorptions decrease and are eventually replaced by a main absorption at  $1022\text{ cm}^{-1}$  at pH 9.4 which is consistent with the presence of kerolite-like materials and/or stevensite-like materials. These observations are mirrored by similar changes in the  $400\text{--}900\text{ cm}^{-1}$  region of the spectrum (Fig. 5c); the amorphous silica absorption at  $800\text{ cm}^{-1}$  is significant at lower pH and this decreases as pH is increased. At the same time, the librational OH absorptions at  $\sim 677$  and  $660\text{ cm}^{-1}$  increase in intensity as pH is increased, again reflective of the growth of a 2:1 layer silicate structure at pH 9.4 (Farmer, 1974b; Fig. 5c).

Thermal analysis of materials formed at an Mg/Si of 0.67 shows a strong low-temperature dehydration event, but a much less pronounced higher-temperature mass loss when compared to samples formed at an Mg/Si of 1. Again, the exception here is the material formed at the highest pH (9.4) which indicates a clear but minor mass loss event due to dehydroxylation at  $\sim 830^\circ\text{C}$ .

For the materials formed at pH 8.7 and 9.0, DTA curves show significant differences in the nature of the products when compared to the same experiments conducted at Mg/Si = 1. Endothermic dehydration is evident at slightly higher temperatures and, for the sample formed at pH 8.7, additional endothermic events occur at  $\sim 287$ ,  $426$ , and  $570^\circ\text{C}$ , with a broad endothermic event occurring from  $\sim 636$  to  $729^\circ\text{C}$  (Table 2). A sharp exothermic event is also evident at  $870^\circ\text{C}$  which we interpret as an indication of a sepiolite-like phase, consistent with FTIR data. The presence of sepiolite-like material may also explain the endothermic events from  $\sim 250\text{--}570^\circ\text{C}$  which have been noted by a number of previous authors (Martin Vivaldi & Fenoll Hach-Ali, 1970; Smykatz-Kloss, 1974; Jones & Galan, 1988). These events are generally thought to reflect a change in bonding energy of structurally-bound  $\text{H}_2\text{O}$  resulting from the formation of sepiolite anhydride at  $\sim 300\text{--}350^\circ\text{C}$  which is stable up to  $650^\circ\text{C}$ , and is consistent with our results (Martin Vivaldi & Fenoll Hach-Ali,

1970). The product formed at pH 9.0, however, shows a lower temperature dehydration at  $\sim 95^{\circ}\text{C}$  and a broad endothermic region displaced to higher temperatures than the corresponding experiment at pH 8.7 (Table 2). Small but distinct exothermic events are present at 815 and  $870^{\circ}\text{C}$  with the latter likely reflecting, again, a minor amount of sepiolite-like material. Lastly, the DTA curve of the product formed in the highest pH experiment is similar to the kerolite-like products discussed above. As noted in other kerolite-like samples, a strong endothermic dehydration is evident at low temperature, with a second event present at  $\sim 280^{\circ}\text{C}$ , which is taken to reflect the evaporation of interlayer water. In addition, similar to other kerolite-like samples, we observe an endothermic inflection that precedes a more intense exothermic event at  $850^{\circ}\text{C}$ . This inflection spans from  $\sim 750$ – $800^{\circ}\text{C}$  and is discussed in more detail below; it is likely to be representative of stevensite-like material exhibiting a phase transition temperature apparently distinct from kerolite-like phases.

To summarize, experiments conducted at low salinity and  $\text{Mg/Si} = 0.67$  are similar to products obtained at  $\text{Mg/Si} = 1$ , but the Mg-silicates are poorly developed. The diminishing intensity of the  $3680\text{ cm}^{-1}$  absorption and less pronounced exothermic phase change evident in DTA indicate that although lower pH products are dominated by amorphous silica and a sepiolite-like phase, the sepiolite-like component is either less abundant or more poorly crystalline than corresponding experiments at  $\text{Mg/Si} = 1$ . At the highest pH, kerolite-like material dominates, but stevensite-like interstratification is present within this phase.

Overall, the initial  $\text{Mg/Si}$  ratio in solution appears to exert strong control on the nature of the Mg-silicate phase and its development. At a given pH, higher  $\text{Mg/Si}$  ratios favour the formation of kerolite-like phases, but lower  $\text{Mg/Si}$  ratios favour the development of amorphous silica and a sepiolite-like product, both at low salinity.

#### High-salinity experiments ( $\text{NaCl}_i = 0.46\text{ mol/kg}$ )

*Variable pH at  $\text{Mg/Si} = 6$ .* Powder XRD data from samples formed at high salinity and high  $\text{Mg/Si}$  display a progressive growth of *hkl* reflections upon increasing pH, similar to low-salinity experiments. Although they are broad, the *hkl* peaks are relatively well defined at each pH level and are consistent with the development of a trioctahedral layer structure.

Calculated differences in XRD patterns between those samples formed at pH 9.0 and 9.4 shows a very broad increase in X-ray scattering intensity in the low-angle region covering apparent *d* spacing values from 10–17 Å (not shown).

XRD data also show the growth of sharply defined peaks corresponding to halite in the products formed at pH 9.0 and 9.4. As the initial NaCl concentration was well below halite saturation in the experiments, it is likely that halite formed upon drying of the samples after filtration and rinsing with de-ionized water. The significance of this observation is discussed in more detail below.

The FTIR analyses show important differences among products formed at different pH and also when compared to identical experiments performed at low salinity. The hydroxyl region shows the development of the  $3680\text{ cm}^{-1}$  band in each of the three products, along with broad absorptions present at  $\sim 3450$  and  $\sim 3250\text{ cm}^{-1}$  (Fig. 3d). However, the intensity of the broad  $3620\text{ cm}^{-1}$  band, an indication of the presence of interlayer  $\text{H}_2\text{O}$ , is weak at pH 8.7, reaches a maximum intensity at pH 9.0, and decreases in intensity at pH 9.4. In general, the  $3680\text{ cm}^{-1}$  band in each of the products is more intense than corresponding products formed at low salinity (Fig. 3a,d).

The lattice vibration region shows more subtle differences with changing pH (Figs 4d, 5d). The primary Si–O vibrations are all centred at  $\sim 1020\text{ cm}^{-1}$ , but the frequency of this peak decreases in wavenumber from 1023 to  $1019\text{ cm}^{-1}$  with increasing pH from 8.7 to 9.4, the significance of which is discussed below. In addition, at pH 8.7 a weak Si–O absorption at  $\sim 1200\text{ cm}^{-1}$  occurs as a shoulder, suggesting the presence of small amounts of sepiolite-like material (Fig. 4d). This shoulder is somewhat less intense than the corresponding experiments conducted at low salinity. The region from  $400$ – $900\text{ cm}^{-1}$  shows the presence of doublets at 660 and  $677\text{ cm}^{-1}$  and 457 and  $473\text{ cm}^{-1}$  arising from hydroxyl stretching which, as discussed above, reflects the development of a trioctahedral Mg-silicate layer structure similar to kerolite or stevensite (Fig. 5d). A weak absorption at  $\sim 800\text{ cm}^{-1}$  indicates the presence of a small amount of amorphous silica at pH 8.7 and this is diminished as pH increases.

Thermogravimetric analysis for all three products shows significant differences and provides even further insight into structural changes with solution composition. All three samples exhibit a low-

temperature weight loss event at  $\sim 100\text{--}130^\circ\text{C}$  which increases in temperature as pH is increased (Fig. 7a). In addition, the two highest pH samples exhibit a second weaker low-temperature dehydration event at  $\sim 230^\circ\text{C}$ . This two-step dehydration at low temperature is also observed for samples formed under low salinity and is consistent with the removal of interlayer water from kerolite-like or stevensite-like structures (Faust *et al.*, 1959; Mackenzie, 1970b; Brindley *et al.*, 1977). In contrast to samples formed at low salinity, however, high-temperature weight loss from dehydroxylation is much more pronounced in each of the three samples and this dehydroxylation shifts from  $\sim 820^\circ\text{C}$  at pH 8.7 to  $\sim 700^\circ\text{C}$  at pH 9.0 and 9.4 (Fig. 7a). This indicates the development of a different material in the higher two pH experiments.

The DTA curves show that the low-temperature

weight loss events are indeed endothermic, consistent with loss of adsorbed and interlayer water (Fig. 7b). The higher temperature region shows more complex behaviour. A broad endothermic event associated with dehydroxylation peaks at  $\sim 818^\circ\text{C}$  for the sample formed at pH 8.7 and this is followed by an intense and sharp exothermic event at  $\sim 850^\circ\text{C}$  (Fig. 7b). The characteristics of this DTA curve are nearly identical to samples formed at low salinity under similar conditions except that the exothermic inflection at  $\sim 730^\circ\text{C}$  is absent in high salinity samples. Therefore we interpret this TGA/DTA response to reflect the dominance of a kerolite-like phase in this sample, with little to no interstratification of stevensite-like material. At higher pH levels, however, the higher temperature region changes significantly. A broad endothermic maximum peaks at  $\sim 680\text{--}690^\circ\text{C}$  and is

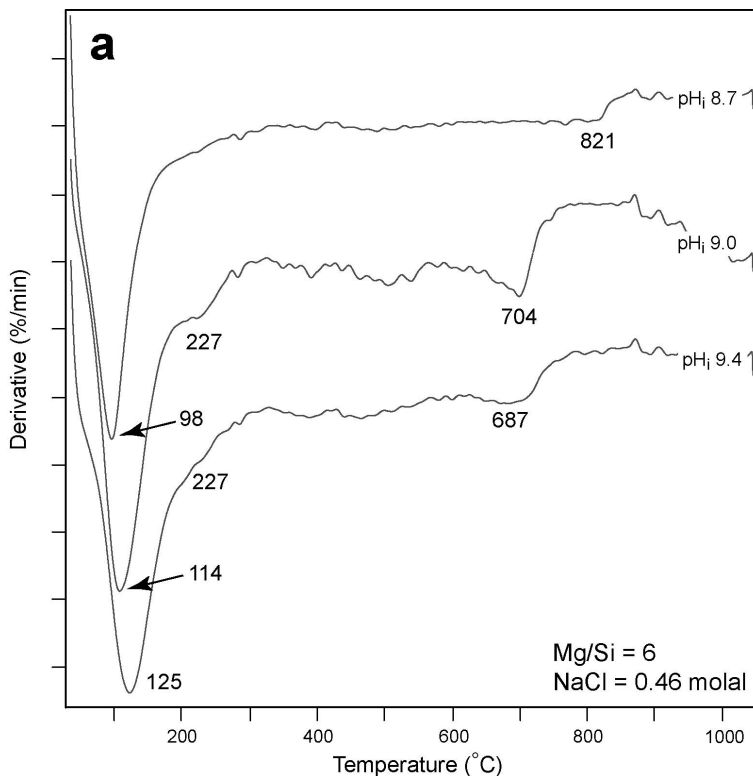


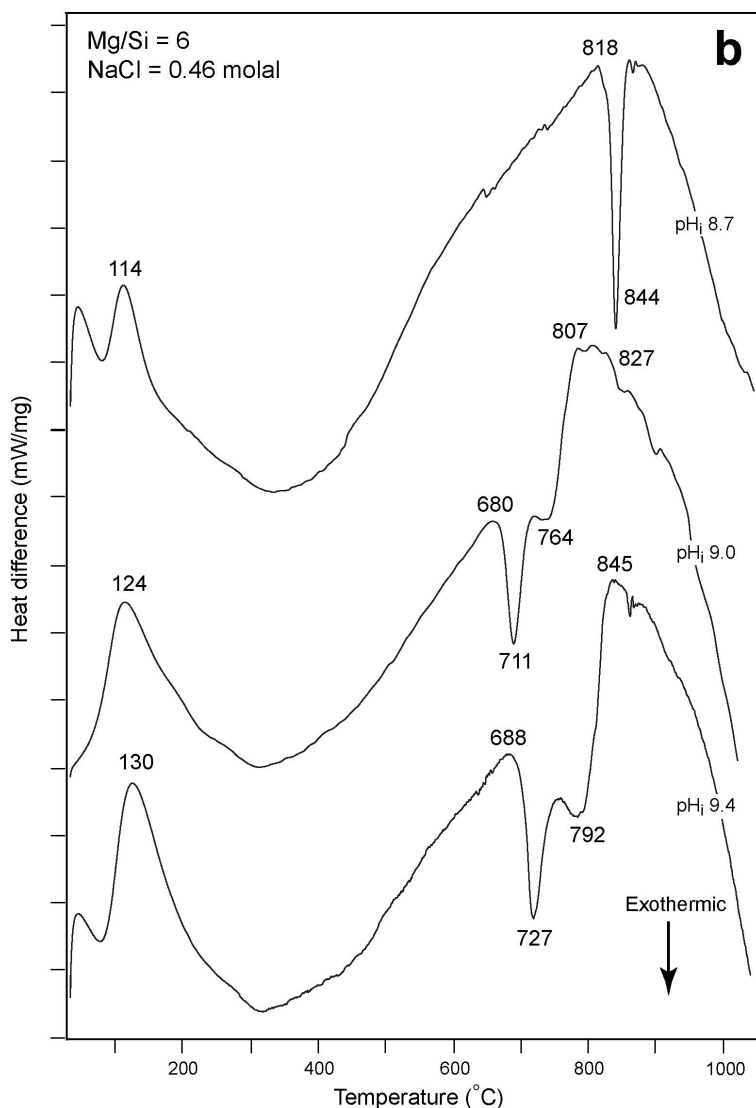
FIG. 7. (a) (*above*) Derivative of the thermal analysis curve (DTG) of products formed at high salinity ( $\text{NaCl} = 0.46 \text{ mol/kg}$ ) and  $\text{Mg/Si} = 6$ . As pH increases under these conditions, products exhibit broader low-temperature weight loss, implying two-step dehydration, as well as a marked shift in dehydroxylation to lower temperatures. (b) (*facing page*) Differential thermal analysis curves of products formed at high salinity ( $\text{NaCl} = 0.46 \text{ mol/kg}$ ) and  $\text{Mg/Si} = 6$ . At all pH levels products exhibit protracted endothermic dehydration and dehydroxylation.

Exothermic phase transitions are shifted from  $\sim 850^\circ\text{C}$  to between  $700\text{--}800^\circ\text{C}$  as pH increases.

followed by two exothermic events, an intense event at  $\sim 710\text{--}730^\circ\text{C}$  and a much weaker event at  $770\text{--}790^\circ\text{C}$ . This is followed by a small endothermic event at  $\sim 800^\circ\text{C}$  which we assign to the melting of halite (Mackenzie, 1970).

In summary, XRD, FTIR and TGA/DTA together indicate the development of Mg-silicate layer structures at all three pH levels under these conditions, but with significant differences between products formed at pH 8.7 and products formed at higher pH. The most notable differences are evident from TGA/DTA curves. The intense exothermic events at high temperature occur as a

single event at  $844^\circ\text{C}$  for pH 8.7, and as an intense event at  $\sim 711\text{--}727^\circ\text{C}$  with a second less intense event at  $\sim 770\text{--}790^\circ\text{C}$  for pH 9.0 and 9.4. We interpret the exothermic event at  $844^\circ\text{C}$  to indicate a product dominantly composed of a kerolite-like phase, consistent with products formed at low salinity, described above. However, for pH 9.0 and 9.4 products, the markedly lower dehydroxylation temperature and lower temperature exothermic event are most consistent with a product dominated by a stevensite-like phase (Faust *et al.*, 1959; Mackenzie, 1970b; Rhouta *et al.*, 2008; Benhammou *et al.*, 2009). The exact temperature



of dehydroxylation and the resulting exothermic phase change vary as a function of particle size and crystallinity. Indeed, a number of authors observe different temperatures for stevensite dehydroxylation and its subsequent phase transition, but these temperatures are consistent with those observed here, falling in the range between  $\sim 700$ – $800^\circ\text{C}$  (Faust *et al.*, 1959; Mackenzie, 1970b; Shimoda, 1971; Takahashi *et al.*, 1997; Rhouta *et al.*, 2008; Benhammou *et al.*, 2009).

Our results imply that the stevensite-like phase and the kerolite-like phase likely exhibit different phase transitions; this is consistent with other thermal studies of these materials. Therefore, we interpret the less intense exothermic reaction (at  $764$  and  $792^\circ\text{C}$ ) present in samples formed at pH 9.0 and 9.4 to indicate the presence of kerolite-like interstratification. As a general rule, DTA studies of mixed-layered clay minerals show similar behaviour to their end-member components, with the important difference being that the associated peak temperatures lie between those of their components (Sudo & Shimoda, 1970; Smykatz-Kloss, 1974). Therefore, the appearance of the small exothermic event at temperatures less than those observed for products dominated by a kerolite-like phase strongly supports interstratification rather than the presence of a discrete phase. Takahashi *et al.* (1997) reported similar observations in their study of synthetic stevensite. The authors formed synthetic stevensite from hydrothermal treatment of mixtures of hydromagnesite, sodium silicate and hydrated silica gel. Their products exhibited nearly identical thermal behaviour to ours; two exothermic events at temperatures between  $\sim 650$  and  $\sim 800^\circ\text{C}$  were evident in DTA curves. On the basis of XRD data collected under different organic and heat treatments, the authors attributed these two events to reflect the presence of a “swelling Mg phyllosilicate” and a “non-swelling Mg phyllosilicate”. The only difference between our samples and theirs is a much lower intensity exothermic peak at  $\sim 770$ – $790^\circ\text{C}$  in our samples which we therefore attribute to a smaller proportion of kerolite-like interstratification.

The presence of dominantly stevensitic material in samples formed at pH 9.0 and 9.4 also suggests that the subtle shift in the position of the main Si–O absorption in the infrared may be used as an additional indicator of stevensite-like versus kerolite-like structure. The main Si–O absorption observed is most likely a composite of the  $a_1^1$  and

$e_1^1$  vibrational modes of the  $(\text{Si}_2\text{O}_5)_n$  hexagonal layer (Russell *et al.*, 1970; Farmer, 1974b); these two vibrations have broadened and coalesced due to extremely small particle size. We have already noted the increased intensity of the  $3620\text{ cm}^{-1}$  band as an indication of the presence of a stevensite-like phase, but the main Si–O absorption also shifts from  $1023\text{ cm}^{-1}$  to  $1019\text{ cm}^{-1}$  in accordance with these changes. Indeed, every other sample described as dominantly kerolite-like in this study exhibits a high-temperature exothermic event at  $\sim 850^\circ\text{C}$  and an Si–O absorption centred at  $\sim 1024\text{ cm}^{-1}$ . Although we cannot identify the exact reason for this shift in absorption frequency, it may well result from increased interaction between the tetrahedral layer and interlayer cations, interlayer hydration or vacancies in the trioctahedral sheet characteristic of expandable trioctahedral 2:1 silicates such as stevensite.

*Variable pH at Mg/Si = 1.* As observed in experiments conducted at low salinity, high-salinity experiments at Mg/Si = 1 also show the disappearance of *hkl* reflections at lower pH as Mg/Si is decreased. Compared to experiments conducted at Mg/Si = 6 discussed in the previous section, XRD data show the dominance of a  $\sim 4\text{ \AA}$  band indicative of amorphous silica, with the progressive growth of *hkl* reflections as pH is increased. As with all *hkl* reflections observed so far, these are consistent with the development of a Mg-silicate layer structure and show no variation in position compared to other experiments where this is observed. Calculated differences in XRD patterns between the samples formed at pH 9.4 and pH 8.7 show a clear increase in X-ray scattering centred at  $\sim 15\text{ \AA}$  and a decrease in the  $\sim 4\text{ \AA}$  band as pH is increased (Fig. 2b). This suggests that the material formed at pH 9.4 contains an appreciable amount of stevensite-like material.

The FTIR data in the hydroxyl stretching region reveal a diminishing intensity of the  $3680\text{ cm}^{-1}$  band at low pH compared to experiments at Mg/Si = 6 where this band is observed for all samples (Fig. 3e). In addition, there is a distinct increase in the intensity of the  $\sim 3620\text{ cm}^{-1}$  absorption at pH 9.4, reflecting the presence of significant quantities of interlayer water, again consistent with XRD data suggesting the presence of a stevensite-like phase. The shape of the multiple OH stretching vibrations from  $3200$ – $3800\text{ cm}^{-1}$  in the sample formed at pH 8.7 is also different from most samples discussed thus far and suggests a number of complex interactions between OH vibrations, giving rise to

a different overall band shape in this region (Fig. 3e).

The lattice vibration region shows a series of absorptions similar to identical experiments conducted at low salinity. At pH 8.7, Si–O absorptions are observed at  $1100\text{ cm}^{-1}$  and a much more pronounced shoulder appears at  $\sim 1200\text{ cm}^{-1}$ ; these indicate the presence of amorphous silica and a sepiolite-like phase, respectively (Fig. 4e). As pH increases, these absorptions steadily decrease and are replaced by a main Si–O absorption centred at  $1018\text{ cm}^{-1}$ . The latter absorption, as discussed above, is consistent with XRD and FTIR spectra in the  $2600\text{--}4000\text{ cm}^{-1}$  region, and indicates the presence of dominantly stevensite-like material at pH 9.4 (Fig. 4e).

As above, the  $400\text{--}900\text{ cm}^{-1}$  region of the spectrum mirrors the changes evident from Si–O absorptions. The amorphous silica absorption at  $\sim 800\text{ cm}^{-1}$  decreases steadily as pH is increased and is replaced by absorptions at  $677$  and  $660\text{ cm}^{-1}$ , consistent with indications of a stevensite-like phase as pH increases (Fig. 5e).

The DTG curves show a low-temperature weight loss that increases in temperature from  $\sim 70^\circ\text{C}$  to  $103^\circ\text{C}$  as temperature increases. The width of this TGA peak also increases significantly for the samples formed at pH 9.0 and 9.4, which may indicate the presence of interlayer water removed at higher temperatures. Higher temperature weight loss is barely evident for the sample formed at pH 8.7, but a small change occurs at  $\sim 900^\circ\text{C}$ . This weight loss event decreases in temperature to  $\sim 814^\circ\text{C}$  and eventually to  $\sim 692^\circ\text{C}$  as pH is increased. These dehydroxylation events are consistent with samples conducted at  $\text{Mg/Si} = 6$  which showed similar events for dominantly kerolite-like material at  $\sim 820^\circ\text{C}$  and for stevensitic material at  $690\text{--}700^\circ\text{C}$ . Therefore, products formed at pH 9.0 are likely to be dominated by a kerolite-like phase and products formed at pH 9.4 are dominated by stevensite.

The conclusions based on TGA (as well as XRD and FTIR) are corroborated by DTA curves (Table 2). The sample formed at pH 8.7 exhibits a number of weak endothermic events from  $126\text{--}426^\circ\text{C}$  (not listed in Table 2), with a broad endothermic maximum evident at  $\sim 650^\circ\text{C}$  before strong exothermic events at  $\sim 840^\circ\text{C}$  and  $871^\circ\text{C}$  (Table 2). The sample formed at the highest pH, on the other hand, exhibits a DTA curve very similar to the same experiment at  $\text{Mg/Si} = 6$ . That is, the

curve confirms the dominance of stevensite-like material; endothermic dehydration at  $\sim 190^\circ\text{C}$  reflects the loss of interlayer water. The sample dehydroxylates at  $654^\circ\text{C}$  and exhibits an exothermic transition at  $\sim 712^\circ\text{C}$ , indicative of a stevensite-like phase, and a second event at  $\sim 790^\circ\text{C}$  indicating a smaller amount of kerolite-like interstratification. The endothermic melting of minor halite is evident at  $\sim 800^\circ\text{C}$ . The sample formed at pH 9.0 is somewhat intermediate between the two samples discussed above. A broad endothermic dehydroxylation peak occurs at  $\sim 600^\circ\text{C}$ , while a marked exothermic event is evident at  $\sim 850^\circ\text{C}$ . Together this indicates the presence of both a sepiolite-like phase and a kerolite-like phase and is consistent with FTIR data discussed above.

In summary, experiments conducted at high salinity and  $\text{Mg/Si} = 1$  indicate the formation of products dominated by a sepiolite-like phase and amorphous silica at pH 8.7. As pH increases, the production of kerolite-like material is favoured, until at pH 9.4 the products are dominated by a stevensite-like phase with minor amounts of kerolitic interstratification apparent from DTA curves.

*Variable pH at  $\text{Mg/Si} = 0.67$ .* Products formed at  $\text{Mg/Si} = 0.67$  and high salinity show more poorly developed *hkl* reflections in XRD than corresponding experiments at higher  $\text{Mg/Si}$ . Although *hkl* peaks are detectable at pH 9.0, for example, these are generally less intense than the corresponding experiment at higher  $\text{Mg/Si}$ . Calculated differences in XRD patterns, however, show increases in X-ray scattering at low angles (not shown). The calculated differences between pH 9.0 and 9.4 show an increase with an apparent *d* spacing at  $\sim 15\text{ \AA}$ . These differences suggest the formation of dominantly stevensite-like material at pH 9.4.

The FTIR spectra of these samples are consistent with XRD results in that the materials lack clear indications of Mg-silicate structures. That is, the spectral features most diagnostic of Mg-silicate layer structures are less obvious in these samples. For example, in the hydroxyl stretching region, the sample formed at pH 9.4 is the only sample that shows an indication of the  $3680\text{ cm}^{-1}$  absorption which arises from OH stretching with trioctahedrally-bound Mg (Fig. 3f). Instead this feature occurs as a weak shoulder and is missing from the experiments conducted at lower pH. Very weak increases in intensity in the  $\sim 3620\text{ cm}^{-1}$  range

could be taken to indicate some interlayer water, but this absorption is perhaps the weakest in all the samples analysed.

The lattice vibration region, however, shows little difference from experiments conducted at Mg/Si = 1 (Figs 4f, 5f). Amorphous silica and sepiolite-like bands are present in the lowest pH samples, but while they are generally weak they are still likely to be present in the pH 9.4 sample given the overall peak asymmetry of the Si–O absorption. The main Si–O absorption is centred at  $1018\text{ cm}^{-1}$ , which we interpret as reflective of stevensite-like material, given our observations above. Again, much like experiments conducted at Mg/Si = 1, the  $800\text{ cm}^{-1}$  absorption is present at low pH and decreases as pH rises (Fig. 5f). The  $660$  and  $677\text{ cm}^{-1}$  absorptions are present in the highest pH sample but, in contrast with the identical experiments at higher Mg/Si, are essentially absent at pH 9.0 (Fig. 5f). Again, this suggests that the formation of a Mg-silicate layer structure is inhibited by low Mg/Si conditions in the parent fluid.

Finally, thermogravimetric analysis shows a strong low-temperature weight loss occurring at  $\sim 80\text{--}120^\circ\text{C}$  as pH is increased (Table 2). However, higher temperature weight loss is not evident from the DTG curves with the exception of the highest pH sample which exhibits a weak loss event at  $\sim 693^\circ\text{C}$ . The lack of clear dehydroxylation in the lower two samples is generally consistent with FTIR and XRD data that show a poorly developed Mg-silicate structure.

The DTA curves for these samples show that at pH 8.7, the sample is most consistent with a sepiolite-like phase and amorphous silica as suggested by FTIR, XRD and comparisons to DTA curves of other samples. The DTA curve is similar, for example, to the corresponding experiment at Mg/Si = 1 which shows weak endothermic events ranging from  $\sim 250\text{--}500^\circ\text{C}$  (not included in Table 2) and a broad region of dehydroxylation ranging from  $\sim 400\text{--}800^\circ\text{C}$ . An exothermic peak can be identified at  $870^\circ\text{C}$  which we assign to a phase transition from sepiolite anhydride to clinostatite, as discussed above. However, a broad exotherm is also present at  $\sim 900\text{--}920^\circ\text{C}$ . This transition is not easily assigned given the systematic behaviour of the materials discussed here; sepiolite, stevensite and kerolite all exhibit phase changes at lower temperatures. The transition from talc to enstatite has been observed to occur at  $\sim 900^\circ\text{C}$  (Mackenzie, 1970b), but there is little evidence that this phase

resembles a crystalline Mg-silicate. A more likely possibility is that the nature of the Mg-silicate gel precipitated under these conditions has undergone continuous structural modification and a general phase change to a phase such as enstatite. Such a process would take place over a range of temperatures, producing a broad exothermic peak. This feature occurs with much greater intensity for the sample produced at pH 9.0, which reflects a generally poorly developed structure which lacks diagnostic Mg-silicate features. In contrast, the DTA curve for the material produced at pH 9.4 is consistent with the formation of stevensite-like material and exhibits low-temperature endothermic dehydration and two high-temperature exothermic events consistent with a small amount of kerolitic interstratification (Table 2). Endothermic melting of halite at  $\sim 800^\circ\text{C}$  is also observed for this sample (not included in Table 2).

In summary, the materials formed at high salinity and Mg/Si = 0.67 exhibit similar trends with pH as those experiments conducted at Mg/Si = 1. However, the products at lower pH exhibit a poorly developed structure more akin to amorphous material rather than Mg-silicate phases with identifiable structure.

## DISCUSSION

### *Relationships between initial phases and crystalline counterparts*

The materials discussed above display a range of structural characteristics that vary systematically as a function of initial experimental conditions. The use of powder XRD, FTIR spectroscopy and TGA/DTA together provide valuable perspective in identifying similarities between synthetic materials and naturally occurring minerals. However, these techniques each lend a different perspective and so a precise description and classification of our synthetic products in the light of all data collected is warranted.

In general, XRD analyses indicate the presence of layer stacking disorder in kerolite-like and stevensite-like products described above. The type of disorder is evident from XRD patterns in two ways. The first is that *hkl* peaks, where present, indicate a distinct asymmetry toward lower apparent *d* spacing (and higher  $2\theta$  angle). This is an indication that the stacking of 2:1 layers is turbostratic; that is, the layers are randomly

displaced along the “a” and “b” crystallographic axes. The second indication of layer stacking disorder is apparent from the lack of clear 001 reflections observable from XRD. We have not observed clear evidence for these reflections in raw data, but by subtracting “background” X-ray scattering at low angles obtained from products composed entirely of amorphous material, we are, in some cases, able to observe increases in low-angle scattering indicative of apparent  $d_{001}$  values consistent with kerolite-like or stevensite-like materials. These features are, in turn, corroborated by FTIR and TG/DTA results. We have modelled this one-dimensional diffraction behaviour with NEWMOD (Reynolds & Reynolds, 1996) under the conditions utilized in our diffraction experiments. These calculations indicate that the mean scattering domain along the  $c$  axis in most samples is one unit cell thick. Where we observe significant growth as a result of background subtraction, the mean scattering domain increases from 1 to  $\sim 1.5$  unit cells which indicates that a larger proportion of 2 unit cell and higher species are present. Together, these observations suggest that factors such as variable hydration from layer to layer are likely to result in the type of disorder we observe from XRD.

Another valuable observation from powder XRD data is the presence of halite in certain samples even after thorough rinsing with de-ionized water. In general, the halite occurs in high-salinity experiments where products are dominated by stevensite-like material. One possible explanation is that the presence of an expandable Mg-rich layer silicate produces appreciable mesoporosity which likely arises between “quasi-crystals” (e.g. Torii *et al.*, 1997; Shirai *et al.*, 2000, 2002). If solution is trapped and held in this mesoporosity then halite is likely to precipitate during the extended drying process to which we have subjected our samples. The fact that halite is not present in materials that appear to be dominated by non-expandable kerolite-like products might also suggest that materials with an expandable nature are closely associated with Na ions. This in turn implies that salinity influences interlayer hydration behaviour as a number of authors have observed for natural smectites (e.g. Slade *et al.*, 1991).

Combining XRD results with FTIR and TGA/DTA suggests that despite the presence of significant layer stacking disorder in many of our products, the 2:1 layers formed are very similar to

those present in naturally occurring phases such as kerolite and stevensite. The development of trioctahedral 2:1 layers is evident from Si–O and Mg–OH vibrations in FTIR as well as the development of a broad but distinct diffraction peak arising from 06,33 reflections positioned at 1.52–1.53 Å, consistent with trioctahedral occupancy. Where we observe evidence for sepiolite-like products in FTIR, most notably from the Si–O vibration positioned at  $\sim 1200\text{ cm}^{-1}$ , diffraction analyses show only a broad scattering feature dominated by amorphous silica, suggesting that this phase dominates where sepiolite-like products have formed. This suggests that the development of “polysome” units and associated inverted tetrahedral components, a diagnostic feature of the sepiolite structure (see discussion in Guggenheim & Krekeler, 2011), occurs on a much smaller scale than products exhibiting 2:1 layer structure.

Thermal analysis provides valuable insight into the structural characteristics of the products described above. Most products exhibit dehydroxylation across a broad temperature range and this indicates an extremely small particle size, in line with XRD results. However, the temperatures at which we observe endothermic maxima corresponding to dehydroxylation are surprisingly consistent with a number of previously reported thermal analyses of Mg-silicate minerals. For example, a number of thermal studies have been conducted on natural and synthetic stevensite and these generally report broad endothermic dehydration at  $\sim 100\text{--}125^\circ\text{C}$  and broad dehydroxylation maxima ranging from  $730\text{--}790^\circ\text{C}$  (Faust *et al.*, 1959; Shimoda, 1971; Takahashi *et al.*, 1997; Rhouta *et al.*, 2008; Benhammou *et al.*, 2009) in agreement with our results. There are far fewer thermal analyses reported on natural kerolite, but Leveille *et al.* (2002) report thermal analyses showing endothermic dehydration at  $\sim 100^\circ\text{C}$  and broad endothermic dehydroxylation at  $\sim 810^\circ\text{C}$ . Together these results are in good agreement with those reported here, notwithstanding experimental differences in heating rate.

In addition, nearly all of our products exhibit well defined exothermic phase transitions at high temperatures that typically follow endothermic dehydroxylation maxima. This behaviour has been noted as a feature that most trioctahedral Mg-silicates exhibit (Faust *et al.*, 1959; Mackenzie, 1970b; Martin Vivaldi & Fenoll Hach-Ali, 1970; Shimoda, 1971; Smykatz-Kloss, 1974;

Leveille *et al.*, 2002; Rhouta *et al.*, 2008; Benhammou *et al.*, 2009). The exothermic phase transitions are systematic in that they consistently occur at characteristic temperatures, and correlate well with independent FTIR and XRD evidence suggesting stevensite-like, kerolite-like or sepiolite-like structures. We therefore use these high-temperature exotherms as sensitive indicators of the presence of specific Mg-silicate structures, as suggested in previous thermal studies of Mg-rich silicates (e.g. Stengele & Smykatz-Kloss, 1998; Smykatz-Kloss, 2002). Again, the temperatures at which these phase transitions occur are consistent with similar reactions reported in the literature.

The exothermic phase transitions are also important in the identification of small amounts of what we interpret as interstratification in 2:1 structures. The highly systematic behaviour of the exothermic phase transitions implies that a physical mixture between components should produce exotherms with no temperature shift (Mackenzie, 1970b; Smykatz-Kloss, 1974). However, we observe small exothermic inflections at temperatures intermediate to those observed for separate components, as discussed above. Our results indicate that dominantly kerolite-like products usually occur with small amounts of stevensite-like interstratification, which increases as pH increases in solution. Conversely, at high ionic strength, we observe small amounts of kerolite-like interstratification in dominantly stevensite-like products. These observations indicate that under the conditions investigated here, the formation of either kerolite-like products or stevensite-like products may be controlled by similar mechanisms. We discuss the implications of this in more detail below.

Finally, thermal analyses of our products yield important insight into hydration behaviour and the influence of dehydration on structural rearrangement. This, in turn, highlights potentially important processes involved in the diagenetic transformations of Mg-silicate phases in natural environments. The products formed in our experiments exhibit a high degree of hydration. We infer, given the dehydration behaviour as a function of temperature, that much of this water is bonded at the surfaces of exceptionally small particles and in “interlayer” spaces. Because most products are consistent with 2:1 layers with a mean coherent scattering domain of 1–2 unit cells, the amount of available surface area and

“interlayer” space is exceptionally high. This explains average total H<sub>2</sub>O values of 15–20 wt.% and higher (Table 2). The removal of this water likely drives structural re-organisation through increased layer stacking. We have previously shown that hydrothermal treatment of similar synthetic Mg-silicate products results in dehydration and increased layer stacking order (Tosca *et al.*, 2011). In addition, random displacements of 2:1 layers with respect to the “*a*” and “*b*” axes are likely to be a remnant of this formation pathway that may well be preserved in ancient Mg-silicates (Tosca *et al.*, 2011). The removal of this interlayer water may indeed be an important step in the development Mg-silicate structures and likely provides insight into the importance of layer stacking disorder in geologic examples of Mg-silicates.

#### *Relationships between aqueous chemistry and Mg-silicate structure*

Table 3 summarizes the dominant products formed in our experiments as a function of initial pH, Mg/Si in solution and salinity (e.g. background NaCl concentration). Re-casting our results in this way illuminates a number of trends between the identity of our products and aqueous chemistry of the parent solution. In the discussion that follows, we seek to explain the origin of these trends in the context of Mg-silicate nucleation and crystallization kinetics.

#### *The influence of pH on incipient Mg-silicate crystallization*

Solution pH has long been recognized as an important control on the Mg-silicate system (e.g. Millot, 1970; Jones, 1986). Consistent with this, our results show that pH is a dominant control on Mg-silicate structure, even between the relatively narrow range from 8.7 to 9.4 (Table 3). More specifically, across this range, it is clear that high pH generally favours the production of 2:1 structures and lower pH favours the production of sepiolite-like products and amorphous silica. This trend is also known from field studies of saline alkaline environments (Jeans, 1971; Stoessel & Hay, 1978; Bodine, 1983; Jones & Weir, 1983; Jones, 1986; Darragi & Tardy, 1987; Calvo *et al.*, 1999; Pozo & Casas, 1999; Galán & Pozo, 2011; Jones & Conko, 2011).

TABLE 3. Summary of products formed in this study (Sep: sepiolite-like; Ker: kerolite-like; Stev: stevensite-like; Am. SiO<sub>2</sub>: amorphous silica. Parentheses indicate the presence of interstratified components).

pH <sub>i</sub>	Mg/Si = 0.67	Mg/Si = 1	Mg/Si = 6
Low salinity (NaCl <sub>i</sub> = 0.0 mol/kg)			
8.7	Sep; Am. SiO <sub>2</sub>	Sep; Am. SiO <sub>2</sub>	Ker (Stev); Sep; Am. SiO <sub>2</sub>
9.0	Sep; Am. SiO <sub>2</sub>	Sep; Am. SiO <sub>2</sub>	Ker (Stev)
9.4	Ker (Stev)	Ker (Stev)	Ker (Stev)
High salinity (NaCl <sub>i</sub> = 0.46 mol/kg)			
8.7	Sep; Am. SiO <sub>2</sub>	Sep; Am. SiO <sub>2</sub>	Ker (Stev)
9.0	Sep; Am. SiO <sub>2</sub>	Ker; Sep; Am. SiO <sub>2</sub>	Stev (Ker)
9.4	Stev (Ker)	Stev (Ker)	Stev (Ker)

There are a number of factors that may lead to the preferential production of 2:1 layer structures at high pH and ribbon structures (e.g. sepiolite) at low pH in Al-free systems. Firstly, a simple thermodynamic analysis of the precipitation reactions of sepiolite, kerolite and stevensite illuminates important dependencies on pH. Based on solubility considerations, Jones (1986) showed that for natural waters, increased pH and solute Mg at decreasing SiO<sub>2</sub>(aq) content should favour the production of kerolite rather than sepiolite. Thus, there is a clear thermodynamic drive in favour of 2:1 structures at higher pH.

A second factor that may lead to the formation of 2:1 structures at high pH may result from kinetic control. Although the rate laws associated with sepiolite and kerolite precipitation are not well constrained, differing dependencies of precipitation rate with pH may well result in a preferential formation of one mineral as opposed to another across a given pH. For example, the condensation of terminal Mg octahedra and Si tetrahedra releases acidity as H<sub>2</sub>O groups are combined to form hydroxyl groups (e.g. Guven & Carney, 1979). This type of reaction is therefore likely to be favoured at high pH, this providing a potential kinetic driving force favouring the precipitation of 2:1 structures at higher pH. Indeed, much more work remains to be done in order to elucidate clearly the mechanistic controls leading to the trends observed here.

Another important trend evident from Table 3 is the preferential formation of stevensite-like products over kerolite-like products at high pH. This trend is evident in the high-salinity experiments (Mg/Si = 6) where solute Na<sup>+</sup> is presumably

a non-limiting component for the formation of the stevensite-like product. In a similar but more subtle way, the amount of interstratification evident in low-salinity experiments seems to increase with pH (from increasing intensity of exothermic inflections near ~750°C from DTA); that is, even under low Na<sup>+</sup> concentrations, higher pH seems to lead to the production of greater amounts of stevensitic material despite its presence as an interstratified component.

What factors could lead to the preferential formation of stevensite-like products over kerolite-like products at high pH? Although the relative kinetics of stevensite and kerolite formation are poorly known, we may speculate based on existing knowledge of 2:1 phyllosilicate growth processes and offer hypotheses to be tested in the future. Clearly the presence of stevensite-like products indicates a greater amount of layer charge resulting from an increased number of vacancies in the octahedral sheet. According to the Hartman-Perdok theory of crystal growth (Hartman & Perdok, 1955a,b,c), a series of strong bonds will be formed between stoichiometric growth units that, for phyllosilicate minerals, are arranged in periodically repeating bond chains (PBCs) (see discussion in Bickmore *et al.* (2001) and Meunier (2006)). Therefore, phyllosilicate crystal growth is presumed to occur along these chains at the edges of 2:1 layers. For trioctahedral phyllosilicates such as kerolite and stevensite, the stoichiometric growth unit involves the attachment three Mg octahedra and two tetrahedral units (e.g. dimers) each on the top and bottom of the octahedral sheet (Bickmore *et al.*, 2001). It is therefore reasonable to assume that octahedral vacancies may arise if the expansion of

the tetrahedral sheet takes place at a higher rate than the expansion of the octahedral sheet. This might be possible especially if the tetrahedral sheet is expanded upon by the addition of silica dimers which, as speciation calculations or our synthetic solutions indicate (not shown), are one of the dominant silica species in solution under these conditions. Thus, under conditions of relatively low pH (e.g. ~8.7), the expansion of the tetrahedral and octahedral sheets occurs via a mechanism that involves roughly equal rates of expansion, producing few octahedral vacancies. As pH is increased, either the rate of tetrahedral expansion increases and/or the rate of octahedral sheet expansion decreases leading to a structure with enough vacancies to necessitate the accommodation of interlayer cations.

Studies of the kinetics of silica oligomerization and brucite kinetics illuminate such a process and provide indirect support for such a hypothesis. Icopini *et al.* (2005) observed that rates of silica oligomerization increase with increasing pH to near neutral pH, but rates are much higher under conditions of higher ionic strength. Pokrovsky & Schott (2004) also showed that brucite precipitation rates are proportional to the square of the rate-determining surface species which they suggested was  $>\text{Mg-OH}_2^+$ . Interestingly, the concentration of this surface species decreases significantly over the pH range of ~8–10, implying that brucite precipitation rates should behave in a proportional manner (Pokrovsky & Schott, 2004). Together then, if octahedral sheet expansion can be taken as analogous to brucite precipitation kinetics, one might expect a similar rate dependence on pH, perhaps lending support to the hypothesis discussed above. In addition to pH controls, the Mg/Si ratio in solution may exert a second control on the relative expansion of the tetrahedral and octahedral sheets. At high Mg/Si ratios, more  $\text{Mg}^{2+}$  would be available relative to Si, perhaps favouring octahedral sheet expansion relative to the tetrahedral sheet. Data collected at low salinity support such a control, but high-salinity experiments still indicate the preferential formation of stevensite at high Mg/Si, pointing to additional kinetic controls at high salinity. Although the data collected in this study do not allow a robust test of this hypothesis, future work should be aimed at elucidating the mechanistic controls on Mg-silicate precipitation kinetics as a function of pH. This, in turn, would root our experimental results in a solid kinetic framework.

### *The influence of ionic strength on incipient Mg-silicate crystallization*

It is also clear from Table 3 that low ionic strength conditions favour the production of kerolite-like products and that stevensite-like products dominate at high ionic strength. This general trend confirms earlier trends based on natural occurrences of Mg-silicate minerals (Stoessel & Hay, 1978; Bodine, 1983; Jones & Weir, 1983; Jones, 1986; Pozo & Casas, 1999; Galán & Pozo, 2011; Jones & Conko, 2011). To a first order, this is easiest to explain given the presence of suitable interlayer cations, in this case  $\text{Na}^+$ , at high salinity, and the absence of  $\text{Na}^+$  at low salinity. However, the presence of small amounts of stevensite-like interstratification with dominantly kerolite-like products indicates that  $\text{Mg}^{2+}$  may act as suitable interlayer cations as they are the dominant cation present under the low-salinity conditions explored here.

Additional factors that may influence Mg-silicate crystallization as a function of salinity may include: (1) a higher rate of silica oligomerization at high ionic strength, and (2) the role of  $\text{Na}^+$  in influencing aqueous silica speciation and complexing. Regarding the former, as discussed above, the formation of stevensite-like products may be linked to higher rates of tetrahedral sheet expansion relative to the octahedral sheet. Much higher rates of silica oligomerization at high ionic strength would also be consistent with this hypothesis (Icopini *et al.*, 2005). This would mean that background ionic strength would also play an important role regardless of whether ionic strength of the solution is increased by constituents that are also suitable interlayer ions (e.g.  $\text{Na}^+$ ).

Related to the second factor, investigations of aqueous solutions containing dissolved silica have pointed to an important role for  $\text{Na}^+$  in influencing the structure of dissolved silicate ions as well as that of their hydration shells (e.g. Felmy *et al.*, 2001; Trinh *et al.*, 2009; Zhang *et al.*, 2011; Pavlova *et al.*, 2012). It may therefore be possible that the preferential formation of stevensite-like products at high NaCl concentrations involves important interactions between dissolved  $\text{Na}^+$  and silica, implying a more active role for  $\text{Na}^+$  beyond simply occupying interlayer spaces as a result of increased layer charge. More work here is necessary in uncovering the role of ionic strength, and separating this from the role played by interlayer ions.

### *The influence of Mg/Si on incipient Mg-silicate crystallization*

A remaining observation evident from Table 3 is the influence of varying Mg/Si in solution on the character of Mg-silicate products. In general, as the Mg/Si ratio in solution is increased, the products generally show improvements in crystallinity. This is evident in FTIR, XRD and thermal analysis and also seems to indicate that the formation of 2:1 layer structures is favoured at high Mg/Si. In addition, at a given pH value and salinity, as Mg/Si is decreased, the sepiolite-like phase and amorphous silica dominate. Although the initial molar ratios of  $\text{Mg}^{2+}$  and  $\text{SiO}_2(\text{aq})$  in solution are varied systematically in all experiments,  $\text{SiO}_2(\text{aq})$  concentrations were purposefully kept at high levels in this study to facilitate the production of enough material for analysis with a number of different analytical methods. It is clear that under conditions suitable for the nucleation of sepiolite-like products, the high initial nucleation rate resulted in the production of enough polysome-like units to be identified in FTIR. However, at low Mg/Si, once the nucleation stage was complete there remained insufficient  $\text{Mg}^{2+}$  in solution to either allow the expansion of the polysomes or nucleate more material. Instead, at low Mg/Si small amounts of sepiolite-like products were produced and when the nucleation process was halted, the remaining  $\text{SiO}_2(\text{aq})$  precipitated to form amorphous silica. Conversely, at high Mg/Si, nucleation of 2:1 units was followed by continuous two dimensional growth facilitated by  $\text{Mg}^{2+}$  in solution. This may also explain the relative increase in crystallinity of products formed at high Mg/Si; sufficient  $\text{Mg}^{2+}$  in solution allowed the expansion of 2:1 sheets and crystal growth once the nucleation stage was complete. It is also interesting to speculate that individual polysome units formed at low pH and low Mg/Si may bear a close resemblance to 2:1 crystal nuclei formed at higher Mg/Si. Indeed the difference in the formation of 2:1 structures versus sepiolite-like structures may depend on the aqueous chemistry that facilitates either crystal growth along the edges of 2:1 units, or the linking of polysomes to form channels filled with zeolitic water, as in sepiolite.

In total, the response of Mg-silicate structures with changing aqueous chemistry has illuminated the general problem of Mg-silicate formation and the distribution of minerals such as stevensite,

kerolite, talc and interstratified varieties of these phases. Some of the trends evident from our study confirm long observed relationships between Mg-silicates identified from field work. However, new observations, particularly the preference of stevensite-like materials at high pH versus kerolite-like materials at somewhat lower pH and the important influence of salinity and Mg/Si offer new insights into mechanisms that could be controlling the distribution of these phases in natural environments. What is obvious from this discussion, however, is that much more work remains regarding the kinetics of Mg-silicate formation and how these processes operate under conditions outside those we have chosen to focus on here.

### *Implications for early and late diagenesis*

The structural continuity between our products and naturally occurring counterparts sheds light on a number of aspects of Mg-silicate formation and diagenesis in lacustrine and peri-marine settings. A number of authors have reported “poorly crystalline” Mg-silicate precipitates and have labeled these phases as either “gels”, “poorly developed clays” or “poorly crystalline silicates” (Millot, 1970; Jeans, 1971; Brindley *et al.*, 1977; Gac *et al.*, 1977; Calvo *et al.*, 1999; Pozo & Casas, 1999; Buey *et al.*, 2000; Polyak & Guven, 2000; Leveille *et al.*, 2000, 2002; Miller & James, 2012). The environments in which these phases are most often found commonly involve fluids at high solute concentration, salinity and pH and most often include speleothems, evaporitic lacustrine environments and saline pore water. The results reported in these studies are in general agreement with ours in terms of structural aspects detectable from XRD, FTIR and thermal analysis. Indeed, the precipitation of a hydrated “poorly crystalline” precursor appears to be a common pathway involved in the *de novo* formation of Mg-silicate minerals from supersaturated solutions. By analogy to our experimental conditions, these phases may be common whenever environmental conditions lead to the supersaturation of these phases from solution and could include processes such as fluid mixing and evaporation.

Our experimental results also indicate that the connection between materials initially precipitated under conditions of high supersaturation and their crystalline counterparts lies in dehydration. As we have shown above, progressive dehydration of 2:1

layers drives increases in layer stacking order and the development of stevensite-like and kerolite-like products. Such dehydration processes may occur in response to wetting-drying cycles, prolonged exposure to high-salinity solutions (i.e. low  $a_{\text{H}_2\text{O}}$ ) or upon burial and heating. Indeed, “gel-dehydration” has been invoked by a number of authors as a mechanism to explain the development of Mg-silicate minerals in evaporative environments and during sediment diagenesis (Gac *et al.*, 1977; Stoessel & Hay, 1978; Darragi & Tardy, 1987; Pozo & Casas, 1999). Gel dehydration was invoked as a main driver for the formation of kerolite associated with microbial mats in speleothems in basaltic caves found in Hawaii (Leveille *et al.*, 2000, 2002). A similar dehydration pathway was suggested to explain stevensite associated with evaporitic deposits from saline lakes (e.g. Gac *et al.*, 1977; Darragi & Tardy, 1987; Pozo & Casas, 1999; Buey *et al.*, 2000). Indeed, gel dehydration has also been implicated in explaining sedimentary textures associated with palygorskite- and sepiolite-bearing ooids formed in palustrine settings influenced by wetting-drying cycles (Miller & James, 2012). The common feature of all of these environments involves initially high supersaturation states with respect to Mg-silicate minerals and environments driving the prolonged and perhaps cyclic dehydration of initially formed products.

A remaining factor that is surely responsible for both early and late diagenetic transformation of initially-precipitated Mg-silicates is time. Our experiments only represent initial stages of precipitation, and unfortunately, extension must be made to assess the role of geologic time. Thermodynamically, more crystalline phases are commonly more stable under a given set of conditions than poorly crystalline counterparts, and so it may be that a strong thermodynamic driving force towards crystalline structure, dehydration and ordering drives diagenetic transformations in geologic time scales. This process is difficult to address in the laboratory, but an understanding of mechanisms involved will aid in extrapolations in time.

Finally, an underappreciated consequence of extensive hydration lies in diagenetic reactions possible upon burial of Mg-silicate-bearing lithologies. The Mg-silicate products formed in this study consistently display high levels of surface and interlayer hydration (e.g. 15–20 wt.%  $\text{H}_2\text{O}$ ). Much of this water is lost at relatively low temperature

(e.g.  $<130^\circ\text{C}$ ) upon thermal analysis which indicates that it is weakly bonded and associated with surfaces. The interlayer hydration is lost at intermediate temperatures (e.g. 300–500°C) and structural water, including hydroxyl, is lost from ~600–850°C. From a geological perspective, this could represent an important source of diagenetic water wherever lacustrine or peri-marine carbonates are deposited. The temperatures at which this water could be released need not correlate to those observed during our thermal analyses; in fact, under geologically relevant burial conditions and heating rates, much of the surface and interlayer hydration could be lost at lower temperatures over geologically significant time intervals. Geological examples of lithologies rich in Mg-silicate minerals are rare; however the implication that significant quantities of water are transferred to the sedimentary sequence upon burial requires that any consideration of the burial diagenesis of lacustrine and peri-marine carbonates take into account the consequences of this fluid source, its chemistry and its interaction with basinal host rocks.

## CONCLUSIONS/FUTURE WORK

To summarize, we have experimentally investigated the initial steps involved in the crystallization of Mg-silicate phases from solution. Our products show clear responses to the pH, Mg/Si and salinity of the initial aqueous solution. By using multiple materials characterization techniques, we have elucidated the structural details of our products and are able to draw comparisons to naturally occurring Mg-silicate minerals such as kerolite, stevensite and sepiolite. Our structural analysis has shown that hydration at particle surfaces and in interlayer sites is an important link between poorly defined Mg-silicate “gels” and crystalline Mg-silicate minerals. More specifically, the loss of interlayer and surface hydration drives increases in layer stacking order along the  $c$  axis in 2:1 layer structures such as kerolite and stevensite. Perhaps more importantly, the large amount of surface and interlayer water associated with newly crystallized Mg-silicate phases has a number of diagenetic consequences. The majority of this water may be released upon shallow burial and may represent a previously under-appreciated source of diagenetic water which may, in turn, affect burial diagenetic reactions and the porosity and permeability of Mg-silicate-bearing sedimentary successions. The

nature of this water, its chemistry and the diagenetic reactions it initiates should be a primary focus of subsequent experimental work on the Mg-silicate system.

The response of our products to aqueous chemical conditions has also allowed the development of testable hypotheses behind the mechanisms of Mg-silicate formation from solution. The nature of Mg-silicate interstratification, pH dependencies, and role of solution Mg/Si in determining mineral products are likely to become clear with further detailed study relating to Mg-silicate precipitation kinetics and further *in situ* studies of precipitation. Together, this will allow the Mg-silicate system to be used to more confidently develop facies models in non-marine and lacustrine environments, more precisely unravel the effects of changing water chemistry on sediment mineralogy, and understand the kinetic controls that have made the system persistently challenging to study.

#### ACKNOWLEDGMENTS

NJT thanks Chris Jeans, Paul Wright and Tony Dickson for valuable discussions, and the Mineralogical Society of Great Britain and Ireland for their support of the Cambridge Diagenesis Conferences. NJT also thanks Angus Calder and Sylvia Williamson for analytical assistance, Javier Cuadros and Manuel Pozo for thoughtful and constructive reviews and Tony Fallick for editorial handling.

#### REFERENCES

- Abtahi A. (1985) Synthesis of sepiolite at room-temperature from SiO<sub>2</sub> and MgCl<sub>2</sub> solution. *Clay Minerals*, **20**, 521–523.
- Benhammou A., Tanouti B., Nibou L., Yacoubi A. & Bonnet J.-P. (2009) Mineralogical and physicochemical investigation of Mg-smectite from Jbel Ghassoul, Morocco. *Clays and Clay Minerals*, **57**, 264–270.
- Bertani R.T. & Carozzi A.V. (1985) Lagoa Feia Formation (Lower Cretaceous), Campos Basin, offshore Brazil: Rift valley stage lacustrine carbonate reservoirs - I. *Journal of Petroleum Geology*, **8**, 37–58.
- Bethke C.M. (2002) *The Geochemist's Workbench, Release 4.0: A user's guide to Rxn, Act2, Tact, React, and Gplot*. University of Illinois.
- Bickmore B.R., Bosbach D., Hochella M.F. Jr., Charlet L. & Rufe E. (2001) In situ atomic force microscopy study of hectorite and nontronite dissolution: Implications for phyllosilicate edge surface structures and dissolution mechanisms. *American Mineralogist*, **86**, 411–423.
- Birsoy R. (2002) Formation of sepiolite-palygorskite and related minerals from solution. *Clays and Clay Minerals*, **50**, 736–745.
- Bish D.L. & Duffy C.J. (1990) Thermogravimetric analysis of minerals. Pp. 96–157 in: *Thermal Analysis in Clay Science* (J. Stucki & D. Bish, editors), CMS Workshop Lectures, **3**, Clay Minerals Society.
- Bodine M.W. (1983) Trioctahedral clay mineral assemblages in Paleozoic marine evaporite rocks. Pp. 267–284 in: *Sixth international symposium on salt*, **1**. Alexandria, Virginia, Salt Institute.
- Brindley G.W., Bish D.L. & Wan H.M. (1977) Nature of kerolite and its relation to talc and stevensite. *Mineralogical Magazine*, **41**, 443–452.
- Bristow T.F., Kennedy M.J., Morrison K.D. & Mrofka D.D. (2012) The influence of authigenic clay formation on the mineralogy and stable isotopic record of lacustrine carbonates. *Geochimica et Cosmochimica Acta*, **90**, 64–82.
- Buey C.d-S., Barrios M.S., Romero E.G. & Montoya M.D. (2000) Mg-rich smectite "precursor" phase in the Tagus Basin, Spain. *Clays and Clay Minerals*, **48**, 366–373.
- Callen R.A. (1984) Clays of the palygorskite-sepiolite group: depositional environment, age and distribution. Pp. 1–37 in: *Palygorskite-Sepiolite. Occurrences, Genesis and Uses* (A. Singer & E. Galan, editors). *Developments in Sedimentology*, **37**.
- Calvo J.P., Blanc-Valleron M.M., Rodríguez-Aranda J.P., Rouchy J.M. & Sanz M.E. (1999) Authigenic clay minerals in continental evaporitic environments. Pp. 129–151 in: *Palaeoweathering, Palaeosurfaces and Related Continental Deposits*, IAS Special Publication.
- Chahi A., Durringer P., Ais M., Bouabdelli M., Gauthier-Lafaye F. & Fritz B. (1999) Diagenetic transformation of dolomite into stevensite in lacustrine sediments from Jbel Rhassoul, Morocco. *Journal of Sedimentary Research*, **69**, 1123–1135.
- Clauer N., Fallick A.E., Galán E., Pozo M. & Taylor C. (2012) Varied crystallization conditions for neogene sepiolite and associated mg-clays from madrid basin (spain) traced by oxygen and hydrogen isotope geochemistry. *Geochimica et Cosmochimica Acta*, **94**, 181–198. doi:10.1016/j.gca.2012.07.01
- Couture R.A. (1977) Composition and origin of palygorskite-rich and montmorillonite-rich zeolite-containing sediments from the Pacific Ocean. *Chemical Geology*, **19**, 113–130.
- Darragi F. & Tardy Y. (1987) Authigenic trioctahedral smectites controlling pH, alkalinity, silica and magnesium concentrations in alkaline lakes. *Chemical Geology*, **63**, 59–72.
- Decarreau A. (1980) Cristallogenèse expérimentale des

- smectites magnésiennes: hectorite, stevensite. *Bulletin de Minéralogie*, **103**, 579–590.
- Decarreau A. (1985) Partitioning of divalent transition elements between octahedral sheets of trioctahedral smectites and water. *Geochimica et Cosmochimica Acta*, **49**, 1537–1544.
- Decarreau A., Vigier N., Pálková H., Petit S., Vieillard P. & Fontaine C. (2012) Partitioning of lithium between smectite and solution: An experimental approach. *Geochimica et Cosmochimica Acta*, **85**, 314–325.
- Deocampo D.M. (2004) Authigenic clays in East Africa: Regional trends and paleolimnology at the Plio–Pleistocene boundary, Olduvai Gorge, Tanzania. *Journal of Paleolimnology*, **31**, 1–9.
- Deocampo D.M., Cuadros J., Wing-Dudek T., Olivez J. & Amouric M. (2009) Saline lake diagenesis as revealed by coupled mineralogy and geochemistry of multiple ultrafine clay phases: Pliocene Olduvai Gorge, Tanzania. *American Journal of Science*, **309**, 834–858.
- Dietzel M. (2000) Dissolution of silicates and the stability of polysilicic acid. *Geochimica et Cosmochimica Acta*, **64**, 3275–3281.
- Eugster H.P. & Jones B.F. (1979) Behavior of major solutes during closed-basin brine evolution. *American Journal of Science*, **279**, 609–631.
- Farmer V.C. (1974a) *The Infrared Spectra of Minerals*. Monograph 4, London, the Mineralogical Society.
- Farmer V.C. (1974b) The layer silicates. Pp. 331–364 in *The Infrared Spectra of Minerals* (V.C. Farmer, editor). Monograph 4, London, the Mineralogical Society.
- Faust G.T., Hathaway J.C. & Millot G. (1959) A restudy of stevensite and allied minerals. *American Mineralogist*, **44**, 342–370.
- Felmy A.R., Cho H., Rustad J.R. & Mason M.J. (2001) An aqueous thermodynamic model for polymerized silica species to high ionic strength. *Journal of Solution Chemistry*, **30**, 509–525.
- Fischer B.E., Haring U.K., Tribolet R. & Sigel H. (1979) Metal ion/buffer interactions. *European Journal of Biochemistry*, **94**, 523–530.
- Frost R.L., Locos O.B., Ruan H. & Klopogge J.T. (2001) Near-infrared and mid-infrared spectroscopic study of sepiolites and palygorskites. *Vibrational Spectroscopy*, **27**, 1–13.
- Gac J.Y., Droubi A., Fritz B. & Tardy Y. (1977) Geochemical behaviour of silica and magnesium during the evaporation of waters in Chad. *Chemical Geology*, **19**, 215–228.
- Galán E. & Pozo M. (2011) Palygorskite and sepiolite deposits in continental environments. Description, genetic patterns and sedimentary settings. Pp. 125–173 in: *Developments in Palygorskite-Sepiolite Research* (E. Galán & A. Singer, editors). *Developments in Clay Science*, **3**, 125–173.
- Guggenheim S. & Krekeler M.P. (2011) The structures and microtextures of the palygorskite-sepiolite group minerals. Pp. 3–32 in: *Developments in Palygorskite-Sepiolite Research* (E. Galán & A. Singer, editors). *Developments in Clay Science*, **3**, Elsevier.
- Guggenheim S., Bain D.C., Bergaya F., Brigatti M.F., Drits V.A., Eberl D.D., Formoso M.L.L., Galán E., Merriman R.J., Peacor D.R., Stanjek H. & Watanabe T. (2002) Report of the Association Internationale pour l'Etude des Argiles (AIPEA) Nomenclature Committee for 2001: Order, disorder and crystallinity in phyllosilicates and the use of the “crystallinity index”. *Clays and Clay Minerals*, **50**, 406–409.
- Guggenheim S., Adams J.M., Bain D.C., Bergaya M., Brigatti M.F., Drits V.A., Formoso M.L.L., Galán E., Kogure T. & Stanjek H. (2006) Summary of recommendations of nomenclature committees relevant to clay mineralogy: report of the Association Internationale pour l'Etude des Argiles (AIPEA) Nomenclature Committee for 2006. *Clays and Clay Minerals*, **54**, 761–772.
- Güven N. & Carney L. L. (1979) The hydrothermal transformation of sepiolite to stevensite and the effect of added chlorides and hydroxides. *Clays and Clay Minerals*, **27**, 253–260.
- Hardie L.A. & Eugster H.P. (1970) The evolution of closed-basin brines. *Mineralogical Society of America Special Publication*, **3**, 273–290.
- Hartman P. & Perdok W.G. (1955a) On the relations between structure and morphology of crystals. I. *Acta Crystallographica*, **8**, 49–52.
- Hartman P. & Perdok W.G. (1955b) On the relations between structure and morphology of crystals. II. *Acta Crystallographica*, **8**, 521–4.
- Hartman P. & Perdok W.G. (1955c) On the relations between structure and morphology of crystals. III. *Acta Crystallographica*, **8**, 525–9.
- Harvie C.E., Moller N. & Weare J.H. (1984) The prediction of mineral solubilities in natural waters: The Na-K-Mg-Ca-H-Cl-SO<sub>4</sub>-OH-HCO<sub>3</sub>-CO<sub>3</sub>-CO<sub>2</sub>-H<sub>2</sub>O system to high ionic strengths at 25°C. *Geochimica et Cosmochimica Acta*, **48**, 723–751.
- Hershey J.P. & Millero F.J. (1986) The dependence of the acidity constants of silicic acid on NaCl concentration using Pitzer's equations. *Marine Chemistry*, **18**, 101–105.
- Hostetler P.B. & Christ C.L. (1968) Studies in the system MgO-SiO<sub>2</sub>-CO<sub>2</sub>-H<sub>2</sub>O (I): The activity-product constant of chrysotile. *Geochimica et Cosmochimica Acta*, **32**, 485–497.
- Icopini G.A., Brantley S.L. & Heaney P.J. (2005) Kinetics of silica oligomerization and nanocolloid formation as a function of pH and ionic strength at 25°C. *Geochimica et Cosmochimica Acta*, **69**, 293–303.

- Iler R.K. (1979) *The Chemistry of Silica: Solubility, Polymerization, Colloid and Surface Properties, and Biochemistry*. Wiley.
- Jans C.V. (1971) The neoformation of clay minerals in brackish and marine environments. *Clay Minerals*, **9**, 209–217.
- Jones B.F. (1986) Clay mineral diagenesis in lacustrine sediments. Pp. 291–300 in: *Studies in Diagenesis* (F.A. Mumpton, editor). U.S. Geological Survey.
- Jones B.F. & Conko K.M. (2011) Environmental influences on the occurrences of sepiolite and palygorskite: a brief review. Pp. 69–83 in: *Developments in Palygorskite-Sepiolite Research* (E. Galan & A. Singer, editors). *Developments in Clay Science*, **3**.
- Jones B.F. & Galan E. (1988) Sepiolite and palygorskite. *Reviews in Mineralogy*, **19**, 631–674.
- Jones B.F. & Weir A.H. (1983) Clay minerals of Lake Abert, an alkaline, saline lake. *Clays and Clay Minerals*, **31**, 161–172.
- Kawano M. & Tomita K. (1991) Dehydration and rehydration of saponite and vermiculite. *Clays and Clay Minerals*, **39**, 174–183.
- La Iglesia A. (1978) Síntesis de la sepiolita a temperatura ambiente por precipitación homogénea. *Boletín Geológico Minero*, **89**, 258–265.
- Leveille R.J., Fyfe W.S. & Longstaffe F.J. (2000) Unusual secondary Ca-Mg-carbonate-kerolite deposits in basaltic caves, Kauai, Hawaii. *Journal of Geology*, **108**, 613–621.
- Leveille R.J., Longstaffe F.J. & Fyfe W.S. (2002) Kerolite in carbonate-rich speleothems and microbial deposits from basaltic caves, Kauai, Hawaii. *Clays and Clay Minerals*, **50**, 514–524.
- Macdonald F.A., Halverson G.P., Strauss J.V., Smith E.F., Cox G., Sperling E.A. & Roots C.F. (2012) Early Neoproterozoic Basin Formation in Yukon, Canada: Implications for the make-up and break-up of Rodinia. *Geoscience Canada*, **39**, no.2.
- Macdonald F.A., Smith E.F., Strauss, J.V., Cox G., Halverson G.P. & Roots C.F. (2011) Neoproterozoic and early Paleozoic correlations in the western Ogilvie Mountains, Yukon. *Yukon Exploration and Geology*, 161–182.
- Mackenzie R.C. (1970a) *Differential Thermal Analysis: Fundamental aspects*. Academic Press.
- Mackenzie R.C. (1970b) Simple phyllosilicates based on gibbsite and brucite-like sheets. Pp. 497–537 in: *Differential Thermal Analysis: Fundamental Aspects* (R.C. Mackenzie, editor), **1**.
- Marion G.M. & Farren R.E. (1999) Mineral solubilities in the Na-K-Mg-Ca-Cl-SO<sub>4</sub>-H<sub>2</sub>O system: A re-evaluation of the sulfate chemistry in the Spencer-Moller-Weare model. *Geochimica et Cosmochimica Acta*, **63**, 1305–1318.
- Martin Vivaldi J. & Fenoll Hach-Ali P. (1970) Palygorskites and sepiolites (hormites). Pp. 553–573 in: *Differential Thermal Analysis: Fundamental Aspects* (R.C. Mackenzie, editor).
- Meunier A. (2006) Why are clay minerals small? *Clay Minerals*, **41**, 551–566.
- Miller C.R. & James N. (2012) Autogenic microbial genesis of Middle Miocene palustrine ooids; Nullarbor Plain, Australia. *Journal of Sedimentary Research*, **82**, 633–647.
- Millot G. (1970) *Geology of Clays*. Springer-Verlag.
- Millot G. & Palausi G. (1959) Sur un talc d'origine sédimentaire. *Comptes Rendus Geologique Français*, 45–47.
- Mitsuda T. & Taguchi H. (1977) Formation of magnesium-silicate hydrate and its crystallization to talc. *Cement and Concrete Research*, **7**, 223–230.
- Noack Y., Decarreau A., Boudzoumou F. & Trompette R. (1989) Low-temperature oolitic talc in upper Proterozoic rocks, Congo. *Journal of Sedimentary Research*, **59**, 717.
- Packter A. (1986) Precipitation of alkaline-earth metal silicate hydrates from aqueous solution: Ionic equilibria, crystalline phases and precipitation mechanisms. *Crystal Research and Technology*, **21**, 575–585.
- Pavlova A., Trinh T.T., van Santen R.A. & Meijer E.J. (2012) Clarifying the role of sodium in the silica oligomerization reaction. *Physical Chemistry Chemical Physics*, **15**, 1123–1129.
- Pokrovsky O.S. & Schott J. (2004) Experimental study of brucite dissolution and precipitation in aqueous solutions: Surface speciation and chemical affinity control. *Geochimica et Cosmochimica Acta*, **68**, 31–45.
- Polyak V.J. & Guven N. (2000) Authigenesis of trioctahedral smectite in magnesium-rich carbonate speleothems in Carlsbad Cavern and other caves of the Guadalupe Mountains, New Mexico. *Clays and Clay Minerals*, **48**, 317–321.
- Pozo M. & Casas J. (1999) Origin of kerolite and associated Mg clays in palustrine-lacustrine environments; the Esquivias Deposit (Neogene Madrid Basin, Spain). *Clay Minerals*, **34**, 395–418.
- Reynolds R.C., Jr. & Reynolds R.C., III (1996) *NEWMOD for Windows*. The calculation of one dimensional X-ray diffraction patterns of mixed-layered clay minerals. Hanover, NH.
- Rhouta B., Kaddami H., Elbarqy J., Amjoud M., Daoudi L., Maury F., Senocq F., Maazous A. & Gerard J.F. (2008) Elucidating the crystal-chemistry of Jbel Rhassoul stevensite (Morocco) by advanced analytical techniques. *Clay Minerals*, **43**, 393–403.
- Russell J.D. & Fraser A.R. (1994) Infrared methods. Pp. 11–67 in: *Clay Mineralogy: Spectroscopic and Chemical Determinative Methods* (M.J. Wilson, editor). Chapman and Hall.
- Russell J.D., Farmer V.C. & Velde B. (1970) Replacement of OH by OD in layer silicates and

- identification of the vibrations of these groups in infrared spectra. *Mineralogical Magazine*, **37**, 869–879.
- Shimoda S. (1971) Mineralogical studies of a species of stevensite from the Obori mine, Yamagata Prefecture, Japan. *Clay Minerals*, **9**, 185–192.
- Shirai M., Aoki K., Miura T., Torii K. & Arai M. (2000) Control of pore structure of trioctahedral magnesium-smectite materials. *Chemistry Letters*, **29**, 36–37.
- Shirai M., Aoki K., Torii K. & Arai M. (2002) Control of mesopore structure of smectite-type materials synthesized with a hydrothermal method. *Studies in Surface Science and Catalysis*, **141**, 281–288.
- Siffert B. & Wey R. (1962) Synthese d'une sepiolite a temperature ordinaire. *Comptes Rendus de l'Academie des Sciences*, **253**, 142–145.
- Slade P.G., Quirk J.P. & Norrish K. (1991) Crystalline swelling of smectite samples in concentrated NaCl solutions in relation to layer charge. *Clays and Clay Minerals*, **39**, 234–238.
- Smykatz-Kloss W. (1974) *Differential Thermal Analysis: Applications and Results in Mineralogy*. Springer-Verlag.
- Smykatz-Kloss W. (2002) Differential thermal analysis of Mg-bearing carbonates and sheet silicates. *Journal of Thermal Analysis and Calorimetry*, **69**, 85–92.
- Stengele F. & Smykatz-Kloss W. (1998) Differential thermal study of Mg-bearing clays from saline lakes of Southern Tunisia. *Journal of Thermal Analysis and Calorimetry*, **51**, 219–230.
- Stoessel R.K. (1988) 25°C and 1-atm dissolution experiments of sepiolite and kerolite. *Geochimica et Cosmochimica Acta*, **52**, 365–374.
- Stoessel R.K. & Hay R.L. (1978) Geochemical origin of sepiolite and kerolite at Amboseli, Kenya. *Contributions to Mineralogy and Petrology*, **65**, 255–267.
- Strese H. & Hofmann U. (1941) Synthese von Magnesiumsilikat-Gelen mit zweidimensional regelmäßiger struktur. *Zeitschrift für anorganische und allgemeine Chemie*, **247**, 65–95.
- Sudo T. & Shimoda S. (1970) Interstratified phyllosilicates. Pp. 539–552 in: *Differential Thermal Analysis: Fundamental Aspects* (R.C. Mackenzie, editor), **1**.
- Takahashi N., Tanaka M., Satoh T. & Endo T. (1994) Study of synthetic clay minerals. 3. Synthesis and characterization of 2-dimensional talc. *Bulletin of the Chemical Society of Japan*, **67**, 2463–2467.
- Takahashi N., Tanaka M., Satoh T., Endo T. & Shimada M. (1997) Study of synthetic clay minerals. Part IV: synthesis of microcrystalline stevensite from hydro-magnesite and sodium silicate. *Microporous Materials*, **9**, 35–42.
- Tettenhorst R. & Moore Jr, G.E. (1978) Stevensite oolites from the Green River Formation of central Utah. *Journal of Sedimentary Petrology*, **48**, 587–594.
- Torii K., Onodera Y., Iwasaki T., Shirai M., Arai M. & Nishiyama Y. (1997) Hydrothermal synthesis of novel smectite-like mesoporous materials. *Journal of Porous Materials*, **4**, 261–268.
- Tosca N.J., Macdonald F.A., Strauss J.V., Johnston J.T. & Knoll A.H. (2011) Sedimentary talc in Neoproterozoic carbonate successions. *Earth and Planetary Science Letters*, **306**, 11–22.
- Trinh T.T., Jansen A.P.J., van Santen R.A., Vondele J.V. & Meijer E.J. (2009) Effect of counter ions on the silica oligomerization reaction. *ChemPhysChem*, **10**, 1775–1782.
- Velde B. (1985) *Clay Minerals: A Physico-Chemical Explanation of their Occurrence*. Elsevier.
- Weaver C.E. & Beck K.C. (1977) Miocene of the SE United States: a model for chemical sedimentation in a peri-marine environment. *Sedimentary Geology*, **17**, 1–234.
- Webster D.M. & Jones B.F. (1994) Paleoenvironmental implications of lacustrine clay minerals from the Double Lakes Formation, southern High Plains, Texas. Pp. 159–172 in: *Sedimentology and Geochemistry of Modern and Ancient Saline Lakes*, SEPM Special Publication, **50**.
- Wilkins R.W.T. & Ito J. (1967) Infrared spectra of some synthetic talcs. *American Mineralogist*, **52**, 1649–1661.
- Williams L.A., Parks G.A. & Crerar D.A. (1985) Silica diagenesis, I. Solubility controls. *Journal of Sedimentary Petrology*, **55**, 301–311
- Wollast R., Mackenzie F.T. & Bricker O.P. (1968) Experimental precipitation and genesis of sepiolite at earth-surface conditions. *American Mineralogist*, **53**, 1645–1662.
- Wright V.P. (2012) Lacustrine carbonates in rift settings: the interaction of volcanic and microbial processes on carbonate deposition. Pp. 39–47 in: *Advances in Carbonate Exploration and Reservoir Analysis* (J. Garland, J. Nielson, S. Laubach, & K. Whidden, editors) Geological Society, London, Special Publications, **370**.
- Zhang X.Q., Trinh T.T., van Santen R.A. & Jansen A.P.J. (2011) Structure-directing role of counterions in the initial stage of zeolite synthesis. *The Journal of Physical Chemistry C*, **115**, 9561–9567.